Chapter – 4

Synthesis, Characterization and application of some metal complexes Derived from 2-(((2-(dimethylamino)ethyl)amino) (4-nitrophenyl)methyl)-3-hydroxynaphthalene-1,4-dione

4.1 Introduction

Researchers are currently focused on finding metallic compounds as metal ions are known to enhance many biological activities by combining with many drugs and organic ligands[1,2]. According to recent reports, metal complexes are widely used in pharmaceutical, medicinal, agriculture, chemical industries and in the treatment of numerous disorders, including both communicable and non-communicable diseases [3–5]. As a result, scientists are now more interested in creating metal complexes with biological properties, metal complexes have been shown in studies to exhibit promise antibacterial, anti-oxidant, anti-tumor, and antidiabetic effects over the past few decades [6–9].

Studies in the fields of drug design and pharmacology clarified how metal complexes and plasma proteins interact. HSA and BSA, two of the most prevalent human proteins, function as transporters in the plasma, respectively. The solubility of metal complexes can be improved and their toxicity can be reduced by interacting with protein molecules [10,11]. Numerous assessments of the literature indicated that DNA binding plays important role in medicinal research. The interaction of metal complexes with DNA and BSA plays a crucial role in the development of metal-based medicine [12–14].

Transition metal complexes play essential roles in biological activities. Both the V(IV) and V(V) oxidation states of vanadium are possible. In this regard, the well-known biological actions of the oxovanadium complexes caught the researcher's attention [15,16]. Various vanadium complexes have been successfully synthesized using a variety of ligands, and their magnetic characteristics, anti-diabetic, anti-inflammatory, and catalytic activity have been assessed in publications [17,18]. But there aren't many reports on the investigation of vanadium-based compounds for anticancer, and antibacterial activities along with DNA/BSA binding studies. There are also several reports for Ni(II) complex with antibacterial, anticancer, and antimicrobial activities [9,19]. Ruthenium (II/III) complexes are believed to exhibit promising anti-cancer and other biological activities. The remarkable affinity of ruthenium complexes to attach to biomolecules and bovine serum albumin has also been shown to make them less hazardous, highly effective, and selective against particular types of cancers [20,21]. The distinctive characteristics of ruthenium complexes result from coordination ligands with metal center [22].

Ligands with different chelating sites in metal complexes also play a crucial role in the rational design of new drugs because they can increase the biological activity of the compounds [23]. A good approach is the introduction of ligands with prior biological activity, which can result in synergistic effects with the metal center or with the complex. FDA approved drugs such as doxorubicin, mitomycin C and Mitoxantrone contain active quinone moiety. As discussed in **chapter 2** mannich bases derived from natural product lawsone enhanced anticancer activity. It also proved that metal complexes of Mannich bases can significantly improve activity as reported in the literature and **chapter 3** [24–26].

Herein, we report metal complexes derived by the reaction of Lawsone, N,N-dimethyl ethylene diamine, and 4-nitrobenzaldehyde. The metal complexes such as V(IV), Ru(II), and Ni(II) were synthesized and characterized by different spectral and analytical techniques. Our research focuses on structure elucidation, structure, and optimization using DFT calculations. Furthermore, the interaction of complexes with biomolecules such as DNA and BSA was studied. In addition, anticancer activity on HepG2 cell line and antimicrobial activities on gram-positive and gram-negative bacteria were screened.

4.2 Result and Discussion

4.2.1 Synthesis of ligand and complexes

The ligand was produced in good yield from the reaction of lawsone with N, N-dimethyl ethylene diamine, and 4-nitrobenzaldehyde using ethanol as a solvent, as shown in **scheme 4.1 (discussed in chapter 2, section 2.2.1).** Various spectroscopic and analytical techniques were used to confirm the ligand's structure.

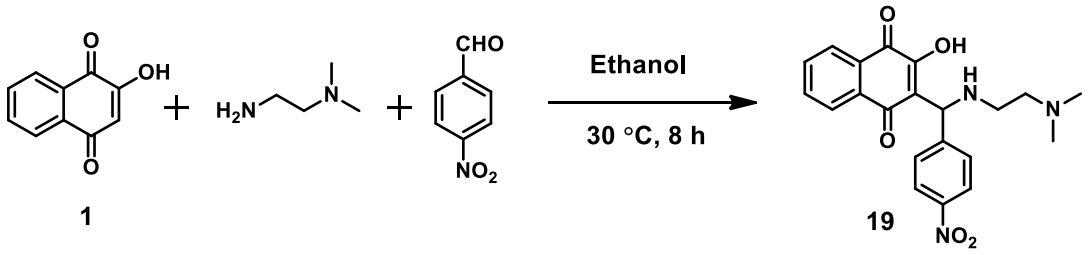

Scheme 4.1 Schematic for the synthesis of 19

Complex 7 was synthesized by adding a methanolic solution of vanadyl sulfate pentahydrate to a suspension of **19** and a clear reaction mass was observed. Then it was refluxed for 8 h and the resulting brown solid was filtered, washed with hot water

followed by methanol, and dried under vacuum. The schematic for the synthesis of **complex 7** is shown in **scheme 4.2.**

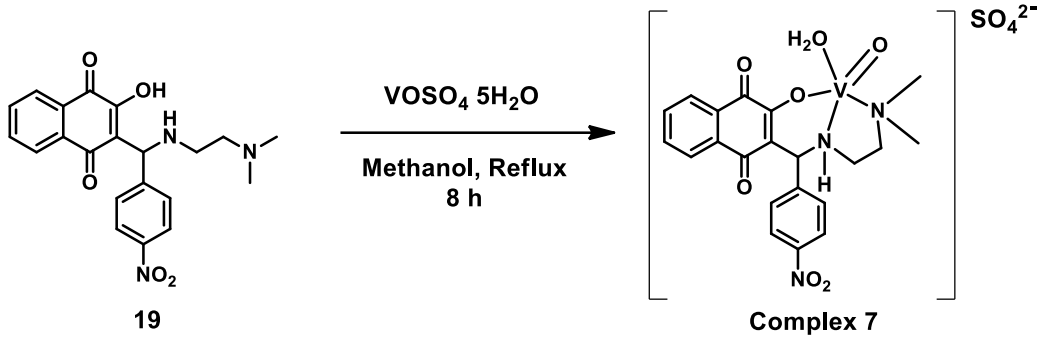

Scheme 4.2 Schematic for the synthesis of complex 7

A similar procedure was followed to synthesize **complex 8** and **9,** a clear solution was observed after the addition of ruthenium chloride or nickel acetate solution to a suspension of **19** and was refluxed for 8 h. Then, 2,2'-bipyridyl dissolved in methanol was added and the resulting dark red solution was refluxed for another 6 hours. Then KPF_6 was added and the mixture was refluxed for another 4 hours. Following complexation, the resultant solution was concentrated under vacuum, yielding radish brown precipitates. The substance was filtered and washed with hot water followed by methanol and dried under vacuum. **Scheme 4.3** depicts a generic schematic for the synthesis of **complexes 8** and **9.** The structure and formation of synthesized complexes were confirmed by FT-IR, UV-Visible, Mass spectroscopy along with DFT calculations

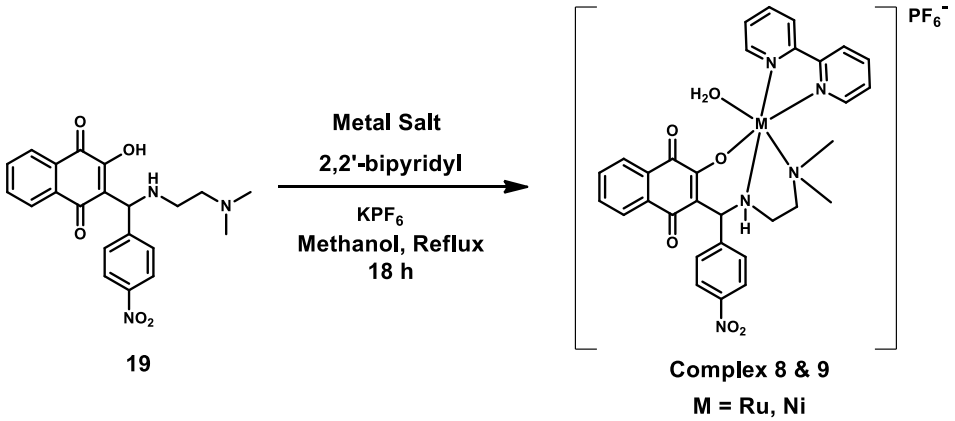

Scheme 4.3 Schematic for the synthesis of complex 8 and complex 9

4.2.2 Spectral characterization

^{1}H NMR spectrum showed singlet for six protons at δ 2.30 ppm of two methyl groups **(figure S4.1).** The aliphatic hydrogens of two methylene groups were observed between

δ 2.55 to 3.02 ppm as multiplet. A singlet was also observed at δ 5.645 ppm due new bond formed between aldehyde, amine, and lawsone. While all aromatic protons were observed in δ 7.54 to 8.19 ppm as double doublet (dd), and triplet of doublet (td).

Similarly, the ^{13}C NMR spectra showed three peaks at δ 184.97, 178.90, and 170.96 corresponding to the naphthoquinone carbonyl group and hydroxyl carbon **(figure S4.2).** The remaining aromatic protons were observed between δ 148.31 to 112.55 ppm. While aliphatic protons were observed between δ 57.93 to 35.19 ppm. These data confirm the structure of desired ligand **19**.

The functional groups involved in the ligand and complexes observed from FT-IR were depicted in **table 4.1**. The FT-IR spectra of **19** showed a broad band at 3440 cm^{-1} for hydroxyl (O-H) group **(figure S4.3).** While weak and broad band stretching frequencies that are observed (3420-3480 cm^{-1}) for metal complexes could be assigned as O-H of water molecules on the surface and coordination sphere [5,27]. The C=O stretching of **19** was observed at 1676 cm^{-1}. This band does not show any shift in the spectra of **complexes 8** and **9** which indicates it does not participate in complexation [28]. However, it shifted to lower frequency of 1635 cm^{-1} in **complex 7** suggesting that the oxygen atom of the carbonyl group may be involved in complexation **(figure S4.4)** [29]. The FT-IR spectra of **19** showed a strong N-H bending frequency at 1527 cm^{-1}, which shifted to a higher frequency to 1565, 1564, and 1546 cm^{-1} for **complex 7, 8,** and **9** respectively. It indicates the participation of nitrogen atoms in complexation [30]. In spectra complex **8** and **9** C=N stretching frequency observed at 1625 and 1629 cm^{-1} confirms the binding of bipyridyl co-ligand **(figure 4S.5 & S4.6)** [31]. The C-O stretching frequency also **complexes 7, 8**, and **9** shifted to a higher frequency as compared to ligand **19,** which confirms the oxygen of hydroxyl group participated in dative bond formation.

The characteristic V=O stretching frequency of **complex 7** was observed at 971 cm^{-1}, which is in the usual range previously reported for the majority of oxovanadium(IV) complexes [31]. The hexafluorophosphate counter-ion found in **complexes 8** and **9** is connected with the significant absorption frequencies at 843 and 844 cm^{-1} observed in the fingerprint regions, which confirms the formation of complexes. In the far IR region, medium intensity bands at 650-550 cm^{-1} and 485-440 cm^{-1} were observed and it can be attributed to M-N and M-O vibrations respectively in all complexes [32,33].

Table 4.1: The FT-IR spectral data of 19 and metal complexes 7-9

Comp.	O-H	C-H	C=O	C=N	N=O	δ N-H	C-O	P-F	M-N	M-O
19	3440	2952	1676	-	1589, 1346	1527	1240	-	-	-
Complex 7	3419	3033, 2708	1635	-	1592, 1345	1565	1289	971 (V=O)	606	444
Complex 8	3480	3075	1675	1625	1601, 1345	1554	1274	843	557	484
Complex 9	3460	2927	1673	1629	1588, 1346	1546	1293	844	650	-

UV-Vis spectra of ligand and complexes were recorded over a wavelength range of 200 nm to 800 nm in DMSO are shown in **figure 4.1**. The absorption band caused by n-π* and π-π* transitions were observed at 452 and 246 nm respectively for ligand **19**. It can be due to oxygen atom of a hydroxyl group in lawsone quinoid ring [34]. These bands showed a blue shift and red shift during metal complexation. This band shifted to 430 nm for **complex 7** and **8 (figure 4.1a & 4.1b)**, while it was observed at 488 nm for complex **9 (figure 4.1c)**. These bands can be assigned as ligand to metal charge transfer (LMCT). This could be another evidence that the ligand is involved in complex formation [35,36].

Likewise, $b_2(dxy) \rightarrow e_{\pi^*}(dxy; dyz)$ transitions of VO^{2+} ion (d-d transition) were observed at 838 nm for **complex 7 (inset of figure 4.1a)**. These bands are typical for distorted octahedral VO^{2+} complex [37,38]. Similarly, d-d transition for **complex 9** was observed at 646 nm further confirm the formation of Ni(II) complex **(inset figure 4.1c).** The π-π* transition 288 and 278 nm for **complex 8** and **9** respectively confirms the participation of bipyridyl ring in complexation of Ru(II) and Ni(II) complexes.

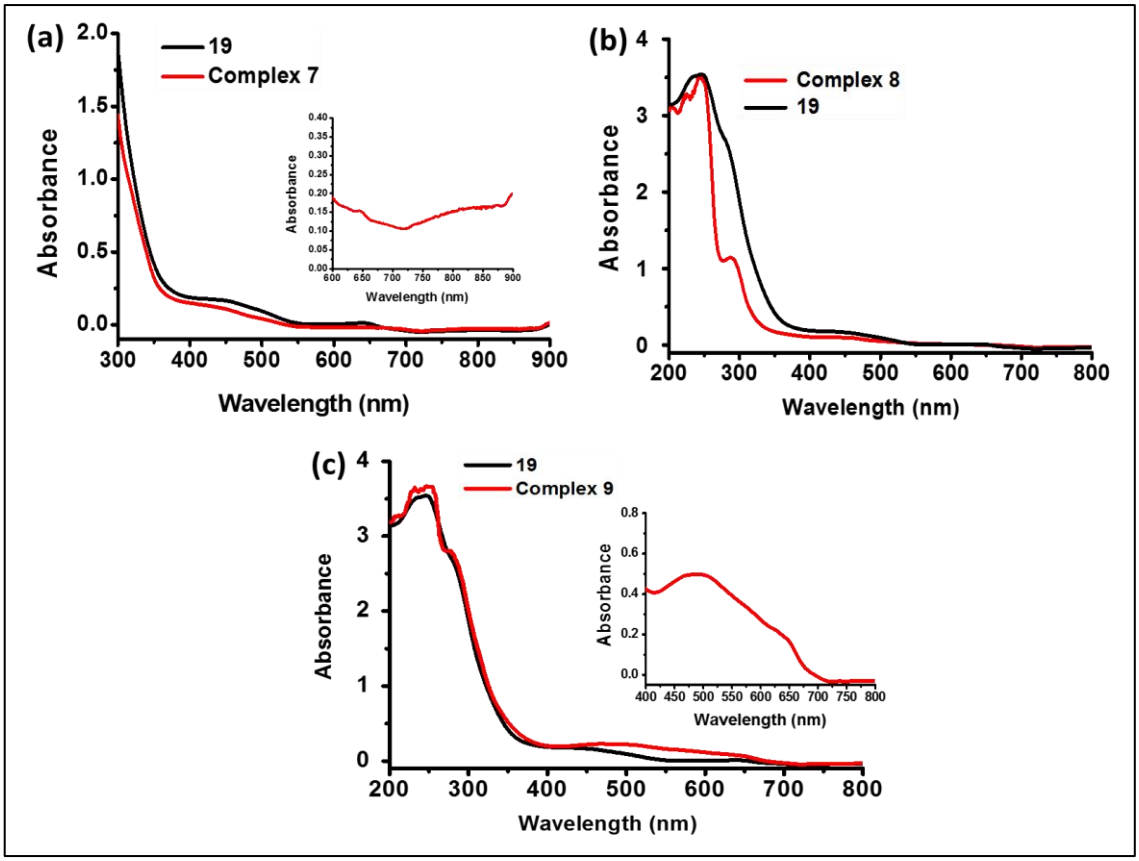

Figure 4.1 UV-visible spectra of (a) complex 7, (b) complex 8, and (c) complex 9

The electrolytic nature of **complexes 7-9** was obtained by recording molar conductance in DMSO (1.0×10^{-3} M) solution. The molar conductance values are 121, 87, and 95 S cm^2 mol^{-1} for **complexes 7-9** respectively. These determined values revealed the 1:1 electrolytic nature of complexes [39].

The ESI-MS was used to examine the mass spectra of **complexes 7** and **8.** Whereas, HRMS was used to obtain mass spectra of **complex 9**. The prominent molecular ion peak was observed at m/z = 479.90 in mass spectrum of **complex 7**, which is similar to formula $[C_{21}H_{22}VN_3O_7]^+$ **(figure 4.2).** There are several other fragmentation peaks at m/z = 324.13 and m/z = 173.03 in spectra of **complex 7** correlated with formula $[C_{17}H_{11}N_2O_5]^+$ and $[C_{10}H_5O_3]^+$ respectively. Similarly, mass spectra of **complex 8** showed m/z = 815 for $[C_{31}H_{30}RuPF_6N_5O_6]^+$ **(figure 4.3)**. While, prominent fragmentation peaks of **complex 8** observed at m/z = 715 and m/z = 526.80 related to formula $[C_{21}H_{22}RuF_6N_3O_6P]^+$ and $[C_{22}H_{23}RuN_3O_6]^+$.

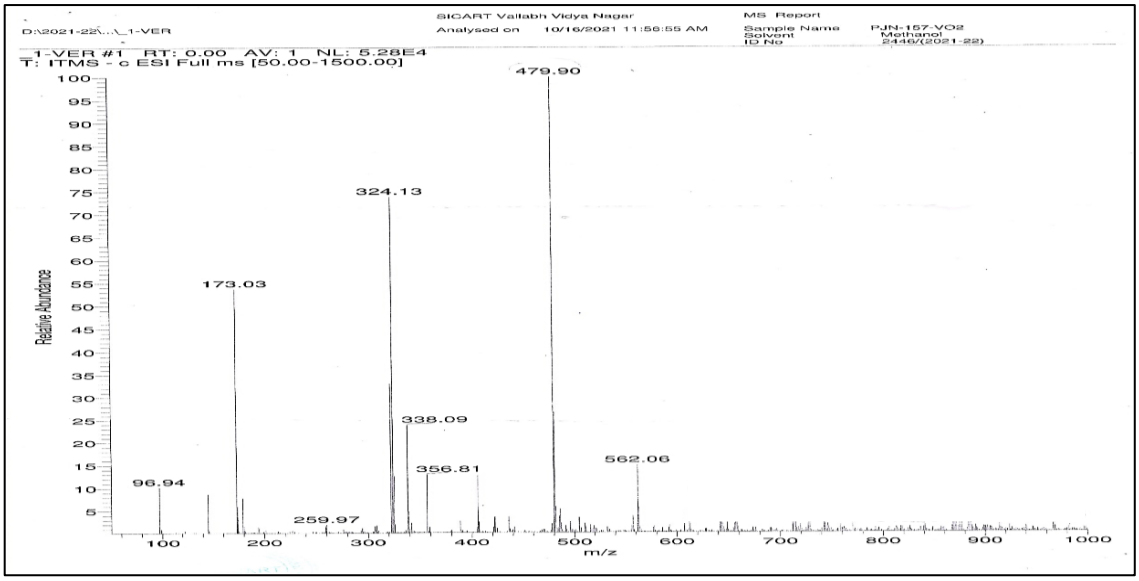

Figure 4.2 ESI-MS spectra of complex 7

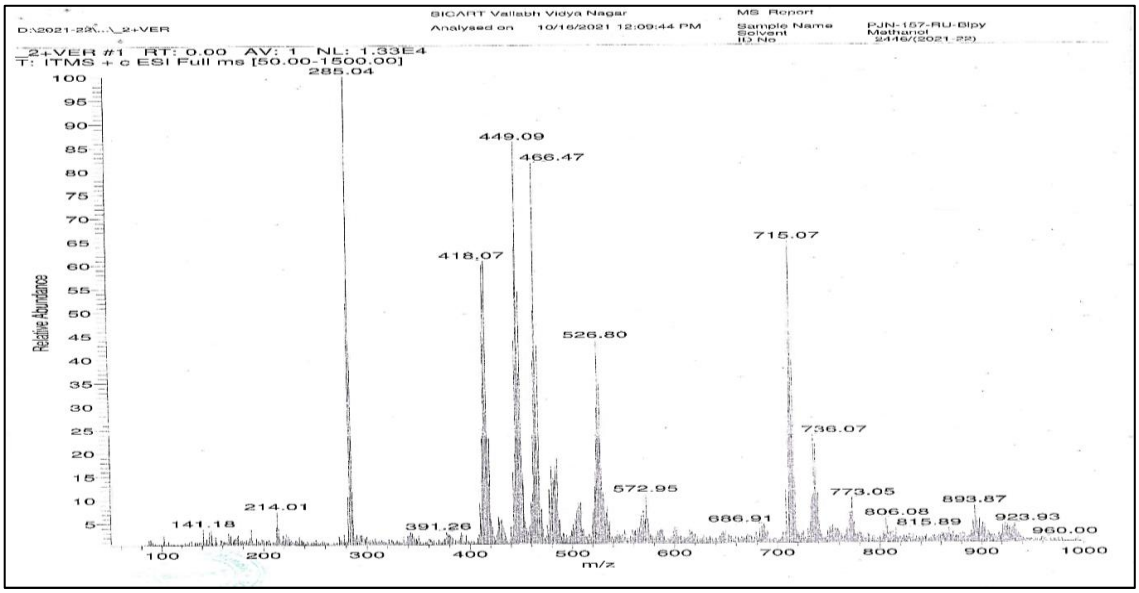

Figure 4.3 ESI-MS spectra of complex 8

On the other hand, mass spectra of **complex 9** show a parent molecular ion peak at m/z = 772, which matches the formula $[C_{31}H_{30}NiF_6N_5O_6P]^+$ **(figure 4.4).** The peak at m/z = 625.30 was ascribed to $[C_{31}H_{30}NiN_5O_6]^+$. The molecular ion peak due to fragmentation of **complex 9** to the corresponding ligand observed at m/z = 396 with formula $[C_{21}H_{21}N_3O_5]^+$. The peak at m/z = 308 was observed due to further fragmentation of ligand **(figure 4.4).** Based on mass measurements, complexes can be classified as hexagonal coordinated system and proves the formation of desired metal complexes.

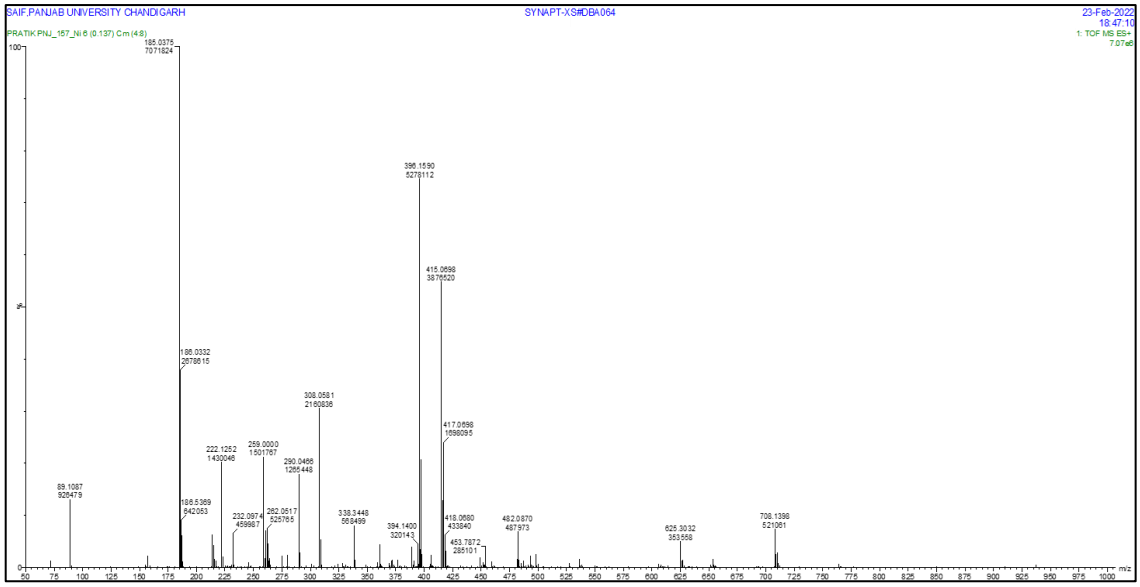

Figure 4.4 HRMS spectra of complex 9

The electron paramagnetic resonance (EPR) spectra of vanadium **complex 7** was recorded in DMSO at 100K. The EPR spectrum **(figure 4.5a)** of **complex 7** exhibited a typical eight line pattern revealing the oxidation state of vanadium as +4. The hyperfine structure corresponds to the interaction of a single unpaired electron (S = 1/2) with a vanadium nucleus (I = 7/2) [40]. The observed g-values and A-values are in order $g_{\perp}$ (2.016) > $g_{\parallel}$ (2.004) and $A_{\parallel}$ (175.79) > $A_{\perp}$ (75.177). This EPR spectra revealed the presence of single vanadium V(IV) center in the complex and unpaired electron is most likely to localize in d orbital of VO(IV) ion [41].

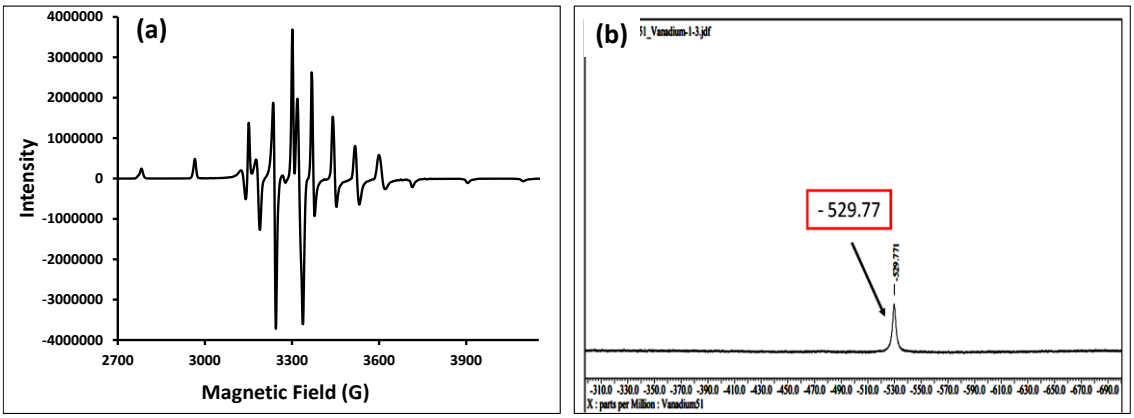

Figure 4.5 (a) ESR spectra and (b) 51V NMR of complex 7

Apart from ESI-MS and EPR, ^{51}V NMR spectroscopy was used to definitively confirm the presence of vanadium in complex **7**. ^{51}V NMR of **complex 7** was recorded in DMSO solution at room temperature. The peak was observed at δ = -529.77 ppm as shown in

figure 11b due to oxidation of vanadium complex to VO(V) species. It further confirms the existence of monomeric vanadium (V) species in solution [42,43].

4.2.3 DFT based Frontier molecular orbital analysis

As discussed in **chapter 3**, molecular orbitals of highest occupied and lowest unoccupied (MOs) are collectively referred to as frontier orbitals (FMOs). The impact of FMO is indispensable in the determination of electronic, optical activity, chemical stability, biological activity, and molecule reactivity.

Table 4.2 HOMO-LUMO energy gap of 19, and complexes 7-9

Parameters	B3LYP/6-31G (d, p) (eV) and LanL2DZ			
	19	**Complex 7**	**Complex 8**	**Complex 9**
HOMO	-5.7533	-6.7125	-3.3616	-6.0373
LUMO	-3.4359	-6.1361	-2.8710	-2.0860
ΔE	2.3173	0.5764	0.4906	3.1769

Because FMOs are significant factors for describing chemical behavior, they were estimated theoretically. The LUMOs are predominantly electron acceptors, while the HOMOs are predominantly electron donors. According to literature, compounds with a small energy gap have higher chemical reactivity, low kinetic stability, and are soft in nature, whereas compounds with a large energy gap have higher chemical reactivity, high kinetic stability, and are hard in nature [44,45]. **Table 4.2** summarizes the details of frontier molecular orbitals as well as the HOMO-LUMO energy gap of ligand **19** and complexes **7, 8,** and **9**. **Complexes 7, 8**, and **9** have negative energies for the FMOs, indicating that the complexes are stable. **Complexes 7** and **8** have a HOMO-LUMO energy gap (ΔE) of 0.5764 eV and 0.4906 eV, respectively, which is substantially lower than ligand **19**. However, the ΔE value for **complex 9** (3.1769 eV) was higher than ligand **19** (2.3173). This might be due to the lower activity of the nickel complex than ligand and other complexes, which may affect the biological activity.

The patterns of the HOMO and LUMO of **complexes 7-9** have been displayed in **figure 4.6a.** The HOMO electron density was delocalized over oxygen atom of hydroxyl group and quinonoid ring of lawsone moiety along with metal and bipyridyl ring for **complex 7** and **8** respectively. This confirms the participation of metal and bipyridyl ring in complexation. However, low or no electron density was observed on bipyridyl ring in

case of **complex 9.** Moreover, the LUMO electron density is localized on nitrobenzene ring in all complexes The chemical reactivity of complexes revealed that ruthenium **complex 8** is highest than other complexes as the HOMO-LUMO gap for the ruthenium **complex 8** was found to be 0.4906 eV. **Table 4.3** lists the important bond lengths and bond angles of metal-ligand bonds for **complexes 7, 8,** and **9** derived from geometry optimization**.** These data suggest that complexes may have distorted octahedral geometry.

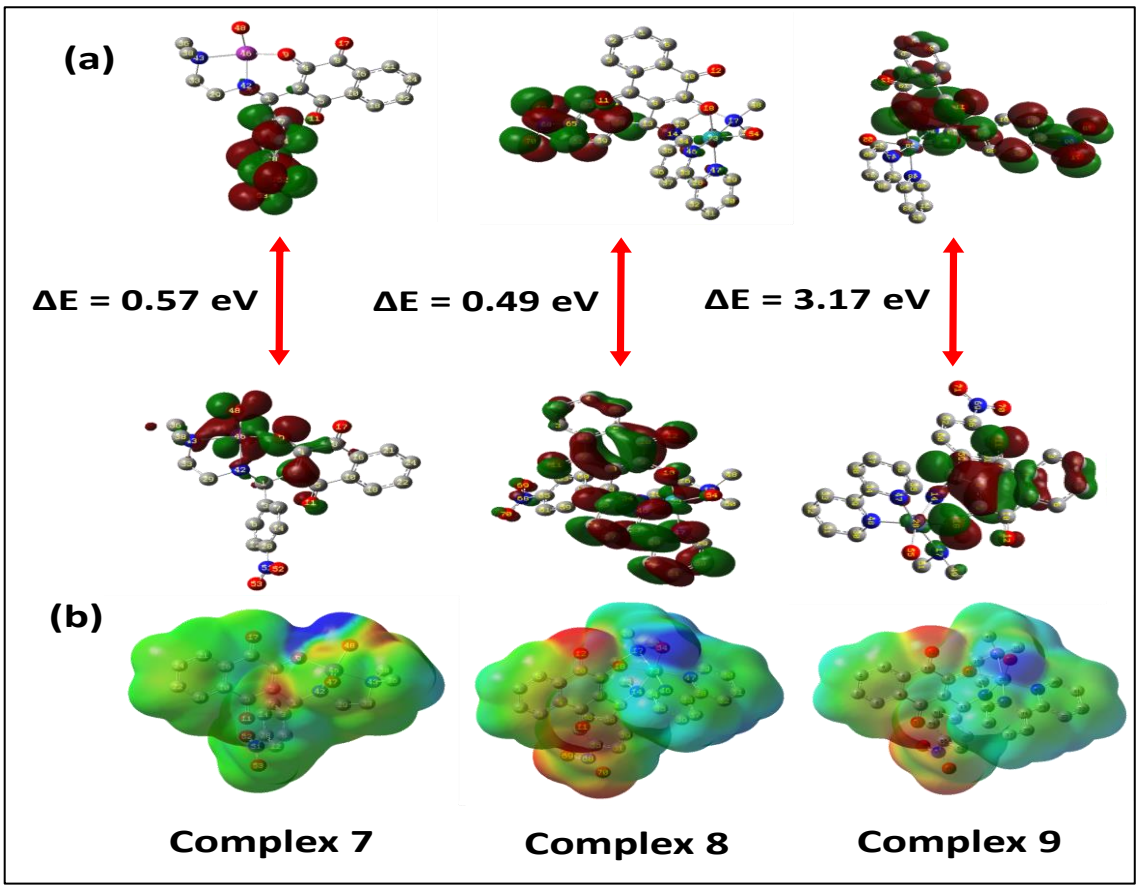

Figure 4.6 (a) HOMO-LUMO pictures and (b) MEP diagram of complexes 7, 8 and 9

As described in chapter 3, MEP is widely used as a reactivity map. It is very important to determine electrophilic and nucleophilic sites based on electrostatic potential, which are represented by red and blue colors respectively [46,47]. The MEP diagram and electrostatic potentials of **complexes 7-9** are represented in **figure 4.6b. Complex 7** has red area near the O atoms of hydroxyl group, naphthoquinone ring, and V=O atom, which symbolizes the acceptor site. The blue region observed near N atoms symbolizes the donor. A similar trend was also observed in **complex 8** and **9** for red region, while blue

region was observed near N atoms of bipyridyl ring and amine region. These data suggest that electron density near oxygen atom of naphthoquinone and metal plays an important role in biological activity.

Table 4.3 Metal ligand bond length and bond angle of complex 7, 8, and 9 under study obtained from geometry optimization

Complex 7			
Bond length (Å)	R(9,46)	O9-V46	1.9562
	R(42,46)	N42-V46	2.1556
	R(43,46)	N43-V46	2.1658
	R(46,47)	V46-O47	1.6082
	R(46,48)	V46-O48	1.8396
Bond angle (in °)	A(9,46,42)	O9-V46-N42	81.3201
	A(9,46,43)	O9-V46-N43	151.5039
	A(9,46,47)	O9-V46-O47	108.5103
	A(9,46,48)	O9-V46-O48	89.8063
	A(42,46,43)	N42-V46-N43	81.3512
	A(42,46,47)	N42-V46-O47	106.638
	A(43,46,47)	N43-V46-O47	98.0505
	A(43,46,48)	N43-V46-O48	86.4038
	A(47,46,48)	O47-V46-O48	118.4236
Complex 8			
Bond length (Å)	R(14,73)	N14-Ru73	2.1181
	R(17,73)	N17- Ru73	2.2875
	R(18,73)	O18- Ru73	2.0547
	R(46,73)	N46- Ru73	2.0589
	R(47,73)	N47-Ru73	2.1074
	R(54,73)	O54-Ru73	2.2207
Bond angle (in °)	A(14,73,17)	N14-Ru73-N17	84.1832
	A(14,73,18)	N14-Ru73-O18	88.6343
	A(14,73,46)	N14-Ru73-N46	92.726
	A(14,73,47)	N14-Ru73-N47	93.2507
	A(17,73,18)	N17-Ru73-O18	80.8329

	A(17,73,47)	N17-Ru73-N47	105.8766
	A(17,73,54)	N17-Ru73-O54	91.2379
	A(18,73,46)	O18-Ru73-N46	94.8006
	A(18,73,54)	O18-Ru73-O54	77.1869
	A(46,73,47)	N46-Ru73-N47	78.5655
	A(46,73,54)	N46-Ru73-O54	90.7332
	A(47,73,54)	N47-Ru73-O54	101.0947
Complex 9			
Bond length (Å)	R(14,28)	N14-Ni28	2.1232
	R(17,28)	N17-Ni28	2.3219
	R(18,28)	O18-Ni28	2.0277
	R(28,47)	Ni28-N47	2.0907
	R(28,48)	Ni28-N48	2.1101
	R(28,55)	Ni28-O55	2.1821
Bond angle (in °)	A(14,28,17)	N14-Ni28-N17	84.2034
	A(14,28,18)	N14-Ni28-O18	87.2948
	A(14,28,47)	N14-Ni28-N47	95.3449
	A(14,28,48)	N14-Ni28-N48	96.9767
	A(17,28,18)	N17-Ni28-O18	82.4625
	A(17,28,48)	N17-Ni28-N48	106.0328
	A(17,28,55)	N17-Ni28-O55	89.2641
	A(18,28,47)	O18-Ni28-N47	92.1652
	A(18,28,55)	O18-Ni28-O55	76.1312
	A(47,28,48)	N47-Ni28-N48	79.344
	A(47,28,55)	N47-Ni28-O55	89.6794
	A(48,28,55)	N48-Ni28-O55	100.0524

4.3 Biological studies

4.3.1 DNA binding studies

To ascertain the degree of binding and the mechanisms of all produced metal complexes toward DNA, the CT-DNA binding of each complex was examined using the UV-visible titration method. The recorded titration spectra of **complex 7-9** in the absence and presence of varying CT-DNA concentrations are shown in **figure 4.7**. The **complex 7** and **9** in DMSO solution displays absorption peak at 270 nm. The incorporation of CT-DNA in metal complexes causes hypochromism in absorption bands. These distinguishing characteristics suggest that **complexes 7** and **9** interact with CT-DNA in an intercalative manner [48]. On the contrary, ruthenium **complex 8** demonstrated hyperchromism **(figure 4.7c)**. It can be due to groove binding of CT-DNA with complex [49].

As described in **chapter 3 (section 3.3.1),** a plot of [DNA]/(ε_A-ε_f) vs. [DNA] gave a slope of 1/(ε_b-ε_f) and an intercept (1/K_b)(ε_b-ε_f), K_b is the ratio of the slope to intercept **(figure 4.7b, 4.7d and 4.7e)**. The intrinsic binding constant (K_b) of complexes was calculated from Wolf –Shimer equation given below **equation 3.1 (chapter 3, section 3.3.1)**[50].

Table 4.4: K_b and *Ksv* values of complexes 7-9

Compound	K_b (M^{-1})	*Ksv* (M^{-1})	ΔG° (KJ mol^{-1})
Complex 7	3.56×10^5	8.5×10^4	-31.675
Complex 8	2.3×10^4	1.29×10^4	-24.882
Complex 9	1.996×10^5	6.3×10^3	-30.196

The binding constant K_b of complexes ranges from 10^4 to 10^5 M^{-1} **(table 4.4)** revealing strong binding of complexes with DNA. **Complex 7** showed good binding affinity may be due to positive charge (+2), which could be owing to electrostatic interactions between the positively charged complex unit and the negatively charged phosphate backbone of CT-DNA double helix [51]. The higher high binding affinity of complex **7** to DNA can also be due to their higher chemical reactivity as it has low ΔE value (0.5764 eV).

Spontaneity/non-spontaneity is a crucial element that has been taken into account while examining the nature of complexes towards DNA. **Equation 3.2** was used to determine Gibb's free energy (ΔG) **(chapter 3, section 3.3.1).**

The observed negative values of ΔG **(table 4.4)** suggests that the binding process of complexes towards DNA was energetically favourable and spontaneous [52].

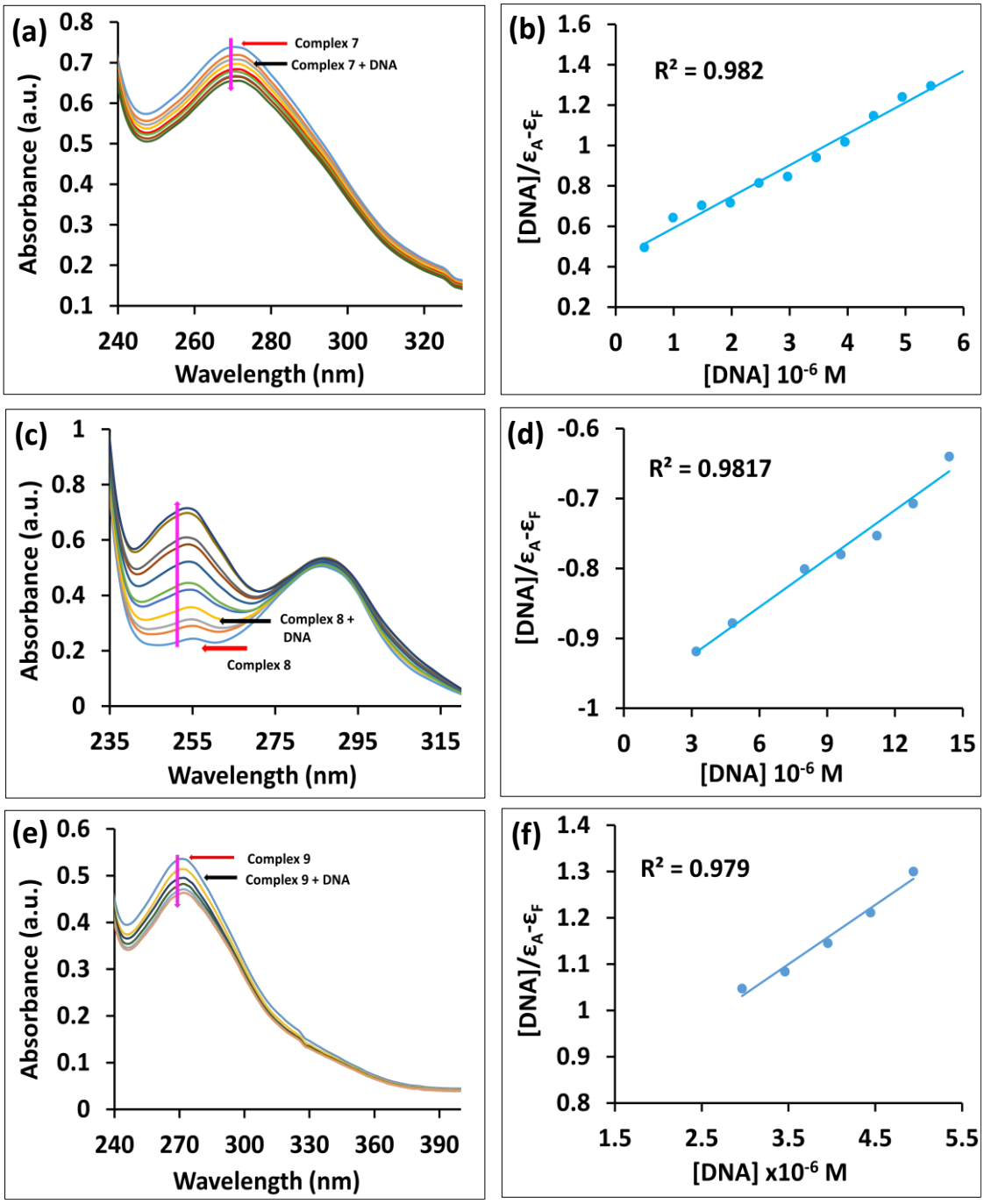

Figure 4.7 UV absorption spectra of (a) complex 7, (c) complex 8 and (e) complex 9 at increasing concentration of CT-DNA. Plots of [DNA]/(εA-εf) vs. [DNA] of (b) complex 7, (d) complex 8, and (f) complex 9.

A competitive binding analysis using a quenching experiment and a fluorescence spectroscopy tool was conducted to further clarify the precise binding mode of the complexes with CT-DNA. Quenching in emission intensity at 609 nm was observed as increasing concentration of metal complexes in DNA-EB solution as shown in **figure 4.8**. This quenching is due to the metal complexes that can intercalate into the DNA model and replace the EB binding site with CT-DNA. This observation implies that all **complexes 7-9** have a great tendency to displace EB from the DNA-EB conjugate and strongly bind with DNA via intercalative or groove binding mode[53]

As discussed in **chapter 3**, the quenching ability of DNA-EB conjugates by complexes was analyzed according to Stern Volmer **equation 3.3 (chapter 3, section 3.3.1).** The K_{sv} values follows the order **complex 7 > complex 8 > complex 9** as depicted in **table 4.4**. This order suggests that **complex 7** gives best results. This might be due to low HOMO-LUMO gap as shown in DFT study and presence of a higher positive charge (+2) in oxovanadium **complex 7.** The magnitude of the binding constant value indicated medium to strong binding strength of complexes with CT-DNA [53].

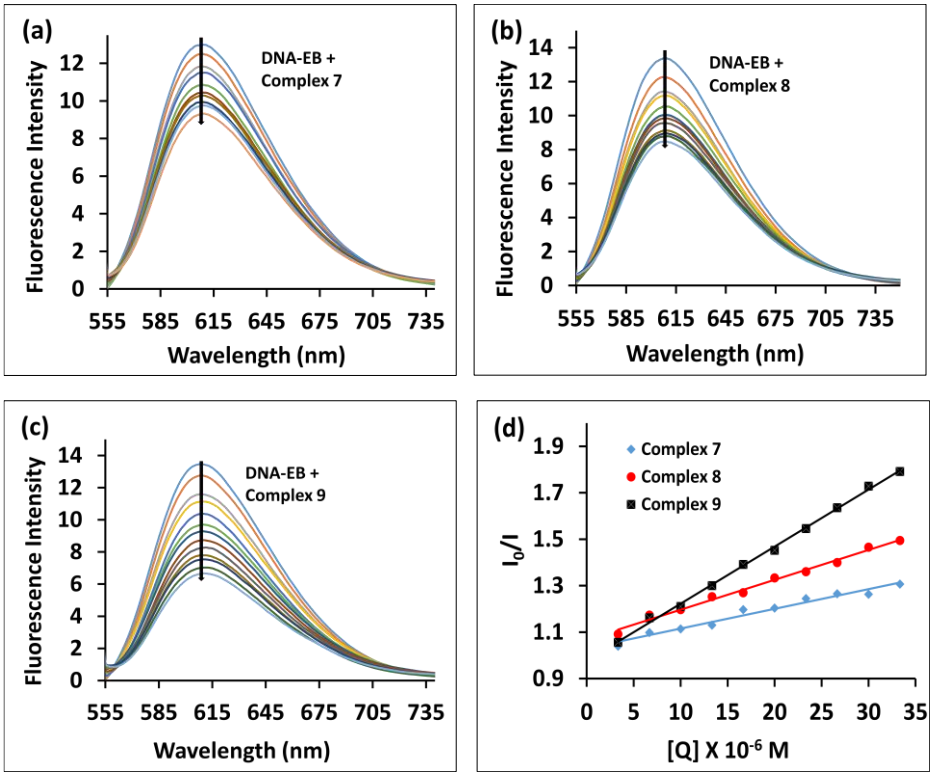

Figure 4.9 Plot of fluorescence emission intensity I *versus* wavelength λ for CT-DNA-EB complex at different concentration of (a) complex 7, (b) complex 8, (c) complex 9 and (d) Stern-Volmer quenching plot of DNA-EB emission in presence of complex 7-9.

4.3.2 BSA binding studies

Albumin is the most abundant protein and BSA is selected as a target protein in our case due to its structural similarity with human serum albumin, easy availability and low cost [54]. The binding properties of BSA with the synthesized compounds have been also studied using fluorescence spectroscopy to confirm whether the BSA-complex formation follows a static or a dynamic quenching mechanism. The successive addition of **complexes 7-9** (a ratio of 0-4.5) to a solution of BSA leads to quenching in fluorescence intensity as shown in **figure 4.10**. Since the secondary structure of BSA changes as a result of binding to the compounds, this quenching is typically attributed to a static mechanism, which suggests the development of a ground state new complex between BSA and metal complexes rather than dynamic collision [22]. This quenching effect was also analyzed by the Stern-Volmer **equation 3.3.** For static quenching interaction, the apparent binding constant K_a and the number of binding sites n could be obtained from the Scatchard equation: $\log((I_0\text{-}I)/I) = \log Ka + n\log[Q]$ [55,56]

The plot of $\log[I_0\text{-}I/I]$ versus $\log[Q]$ for all the **complexes 7-9** is linear as shown in **figure 4.10d.** The binding constant (K_a) and the number of binding sites per albumin (n) have been obtained from the intercept and slope respectively **(table 4.5).** There was just one class of independent binding sites for **complexes 7-9**, according to the values of n, which are about in the range of 0.8 to 1.4. **Complex 8** showed higher binding to BSA compared to **complexes 7** and **9** may be due to static and dynamic quenching mechanism [57].

Table 4.5 K_a and Ksv values of complexes 7-9

Compound	K_a (M^{-1})	Ksv (M^{-1})	n
Complex 7	1.66×10^6	3.42×10^8	1.4
Complex 8	8.21×10^7	1.11×10^6	1.36
Complex 9	2.16×10^5	2.86×10^5	0.812

The values of the Stern Volmer quenching constant K_{sv} obtained for **complexes 7-9** is in order of **complex 7 > complex 8 > complex 9.** The Stern–Volmer plot for the quenching of BSA fluorescence by **complexes 7-9** is shown in **figure 4.10e**. Additionally, the double logarithm plot's linear behavior suggests that just one of the protein's tryptophan residues is interacting with the complexes. The lower value of K_a and K_{sv} for **complex 9** might be due to higher ΔE values as determined earlier by DFT calculations.

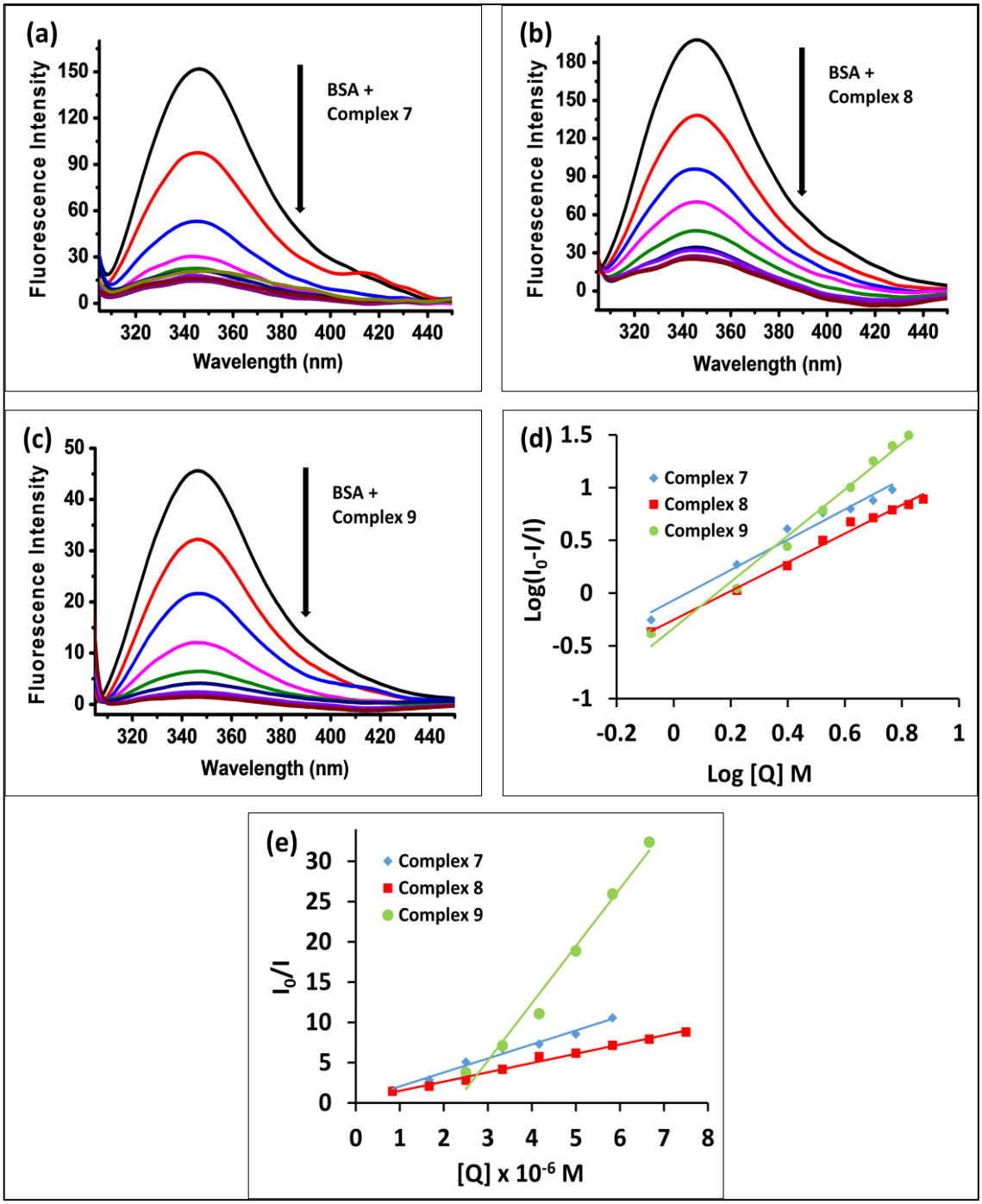

Figure 4.10 (a, b, c) plot of fluorescence emission intensity I *versus* wavelength λ (d) double logarithmic plot for the quenching of BSA fluorescence and (e) Stern Volmer quenching plot of BSA emission in presence of complexes 7-9

All spectroscopic method clearly proved that the **complex 7** and **complex 8** exhibits the strongest binding with both DNA and BSA.

4.3.3 Cytotoxicity

The resazurin dye-based test was used to assess the cytotoxicity of **complexes 7-9** and **19** on HepG2 cells. All the compounds were screened from 15.6 μM to 1000 μM concentrations. The cell viability obtained for HepG2 cells exposed to complexes for 72 h. **Figure 4.11** displays the plot of percent viability vs. compound concentration from the resazurin dye-based test of **complexes 7-9** and **19**. A very steep decline in the cell viability was observed in complex **7** and **9** at 250 μM of concentration. While **complex 8** showed a steep decline at 62.5 μM of concentration. This data was used to calculate IC_{50} values for all the compounds. The cytotoxicity data of complexes are depicted **table 4.6.**

Table 4.6 IC_{50} values of Complexes

compound	19	Complex 7	Complex 8	Complex 9
IC_{50} (μM)	169±0.63	141.27±1.05	52.05 ±0.73	184.8 ±0.85

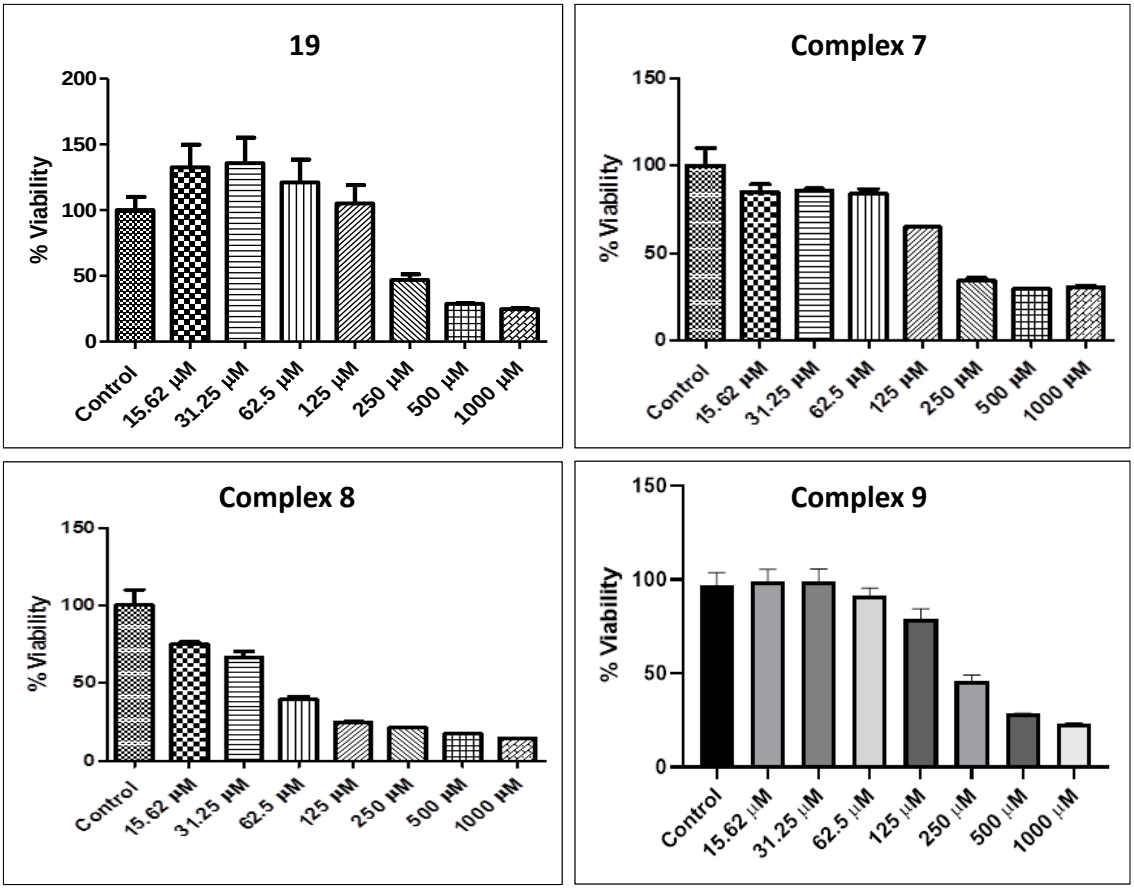

Figure 4.11 The plot of % viability *vs* concentration of compound obtained from cytotoxicity assay of ligand 19 and complexes 7-9.

The obtained cytotoxic values are compared with **19**. It was found that **complex 8** has higher cytotoxicity. Whereas, complex **9** showed lower cytotoxicity as compared to its precursor ligand **19** as evident by their DFT study. The obtained IC_{50} value of complex **8** is comparable with IC_{50} value of cis platin 15.9 μM on HepG2 cell line [58].

4.3.4 Antimicrobial activity

Chloramphenicol was used as positive control to test the **19** and its **complexes 7-9** to see how well they inhibited the growth of both gram-positive and gram-negative bacteria. **Table 4.7** provides a summary of the test outcomes.

Table 4.7 Effect of complexes 7-9 and ligand 19 on the test microorganism

Compound	Dose (μg/mL)	E. coli	P. aeruginosa	S. aureus	B. subtilis
19	10	NA	NA	NA	9 ± 0.7
	50	NA	NA	NA	10 ± 0.9
	100	NA	NA	NA	11 ± 0.3
Complex 7	10	NA	NA	NA	NA
	50	NA	NA	NA	10 ± 0.2
	100	NA	NA	NA	12 ± 0.3
Complex 8	10	NA	NA	11 ± 0.8	9 ± 1.0
	50	NA	NA	15 ± 0.4	12 ± 0.6
	100	NA	NA	18 ± 0.9	15 ± 0.7
Complex 9	10	NA	NA	NA	NA
	50	NA	NA	NA	NA
	100	NA	NA	NA	NA
Chloram-phenicol	30	21 ± 1.1	10 ± 0.4	26 ± 0.8	26 ± 0.7

The maximum activity against B. subtilis (15 ± 0.7 mm) and S. aureus (18 ± 0.9 mm) was shown by the Ru(II) **complex 8**, whereas **complex 7** and **19** showed activity against B. subtilis. **Complex 9** exhibited no inhibition against any bacteria indicating the inactivity of a compound. It was discovered that **complex 7** has moderate antibacterial action against B. subtilis only. In this work, it was found that neither **19** nor complexes were active against gram-negative bacteria. Overall, the test findings showed that the produced **complexes 7** and **8** outperformed the **19** in terms of antibacterial efficacy and comparable with standard drug.

4.4 Experimental

4.4.1 Material and methods

Ruthenium chloride, Vanadyl sulfate pentahydrate were purchased from Sigma-Aldrich, Mumbai, India and N, N-dimethyl ethylene diamine was procured from TCI, India. Nickel acetate was purchased from Loba Chemie, India. 4-nitro benzaldehyde, Calf thymus DNA (CT-DNA), trisodium citrate ($Na_3C_6H_5O_7$), Ethidium Bromide (EB) and bovine serum albumin (BSA) were procured from Sisco Research Laboratory (SRL) Mumbai, India. HepG2 cell line was procured from National Center for Cell Science (NCCS) Pune, India. 5 mM trisodium citrate and 50 mM NaCl were dissolved in doubly distilled water to prepare buffer solution. The pH of buffer was adjusted to 7.3 by using dilute NaOH.

The description of instruments used for FT-IR, NMR, elemental, and Mass analysis is depicted in **chapter 2 (section 2.3.1)**. JOEL 600 MHz NMR was used to record ^{51}V NMR of vanadium complex. ESR spectrum was recorded using Bruker Biospin ESR spectrometer operating with X-band (9.6 GHz) microwave at 100K temperature in a suitable solvent. Thermogravimetric Analysis (TGA) of ligands and complexes was performed TG–DTA 6300 INCARP EXSTAR 6000 at a heating rate of 10°C/min in the temperature range of 30–500°C, nitrogen atmosphere was maintained throughout the measurement. UV-Visible spectra were recorded on Agilent UV Cary 60 and Perkin Elmer Lambda-35 dual-beam spectrophotometer. Fluorescence spectra were recorded in solution on JASCO FP-6300 fluorescence spectrophotometer. Powder XRD was recorded on Bruker D2-Phased instrument with Lynux-eye detector.

4.4.2 Synthesis of 19

The **19** was synthesized according to the procedure reported in **chapter 2**. Briefly, to a suspension of lawsone (**1,** 2 mmol) in absolute ethanol (6 mL), N, N-dimethyl ethylene diamine (2.2 mmol) was added and allowed to stir for 15 minutes. Then, 4 nitro benzaldehyde (2.4 mmol) was added to the reaction mixture and the resulting reaction mixture was left stirring at 30 °C for 8 h. The progress of the reaction was monitored by TLC. The obtained solid product was filtered and washed with water, ethanol followed by diethyl ether. The isolated product was dried in a vacuum oven. The crude product

was recrystallized in ethanol. The schematic for synthesis is shown in **scheme 4.1.** The crude product was recrystallized in ethanol.

2-(((2-(dimethylamino)ethyl)amino)(4-nitrophenyl)methyl)-3 hydroxynaphthalene-1,4-dione (19)

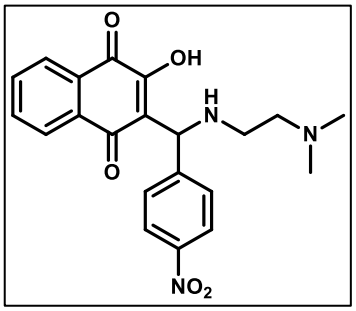

Reddish brown; Yield: 76%; M.P: 140-142 ^{o}C

^{1}H NMR (DMSO-*d6*, 400 MHz) δ (ppm): 8.18 (2H, d, *J*=8.8 Hz), 7.88 (1H, dd, *J*=6.8 Hz, *J*=0.8 Hz), 7.80 (3H, d, *J*=1.2 Hz), 7.68 (1H, td, *J*=6.8 Hz, *J*=1.2 Hz), 7.56 (1H, td, *J*=6.8 Hz, *J*=1.2 Hz), 3.02 (1H, t, *J*=6.0 Hz), 2.94 (1H, m, *J*=8.6 Hz), 2.65 (1H, t, *J*=6.8 Hz), 2.58 (1H, m, *J*=8.6 Hz), 2.30 (6H, s). **^{13}C NMR** (DMSO-*d6*, 100 MHz) δ (ppm): 35.19, 43.30, 44.83, 55.43, 57.93, 112.55, 123.77, 124.30, 125.55, 125.80, 128.87, 129.44, 131.29, 131.89, 134.23, 135.13, 146.84, 148.31, 170.96, 178.90, and 184.97. **IR (KBr) cm^{-1}**: 3440 (O-H), 2952 (=C-H), 2850 (C-H), 1676 (C=O), 1589 (N=O), 1527 (δ N-H), 1346 (N=O), 1240 (C-O), 1110 (C-N). **ESI/MS** 396.17 $[M+1]^{+}$ calculated for $C_{21}H_{21}N_3O_5$. **UV-Vis (DMSO) λ/nm, (log ε):** 246 (5.072), 452 (3.737). **Molar conductance:** 11.3 S cm^2 mol^{-1}

4.5.3 Synthesis of complexes 7-9

The methanolic solution of vanadyl sulfate pentahydrate (1 mmol) was added dropwise to a suspension of **19** (1 mmol) in methanol (15 mL) and refluxed for 8 h. The resulting brown solid was filtered, washed with hot water followed by methanol, and dried under vacuum. The Schematic for the synthesis of **complex 7** is shown in **scheme 4.2.**

Complex 7

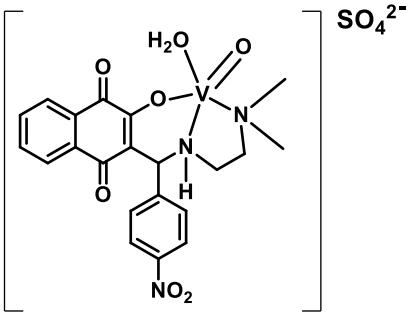

Brown powder; Yield: 72%; M.P: >250 ^{o}C

IR (KBr) cm^{-1}: 3419 (O-H), 3033 (C-H), 2708 (C-H), 1635 (C=O), 1592 (N=O), 1565 (δ N-H), 1345 (N=O), 1289 (C-O), 1133 (C-N), 971 (V=O), 606 (V-N), 444 (V-O) **(figure S4.4), ESI/MS** 479.90 $[M+1]^+$ For $C_{21}H_{22}VN_3O_7$ **(figure 4.2)** Anal. Calculated %: C, 52.62; H, 4.63; N, 8.75. Found %: C, 51.08; H, 4.40; N, 8.79 **UV-Vis (DMSO) λ/nm, (log ε):** 430 (3.187), 838 (1.740). **Molar conductance:** 121 S cm^2 mol^{-1}

Ruthenium chloride (0.5 mmol) or nickel acetate (0.5 mmol) dissolved in methanol was added dropwise to a suspension of **19** (0.5 mmol) in methanol (15 mL) and refluxed for 8 h. Then 2,2'-bipyridyl dissolved in methanol was added and resulting dark red solution was refluxed for 6 h. Then KPF_6 (0.5 mmol) was added and further refluxed for 4 h. After complexation resulting solution was concentrated under vacuum and radish brown precipitates was obtained. The obtained solid was filtered and given washing with hot water followed by methanol, and dried under vacuum. The general schematic for the synthesis of **complexes 8** and **9** are shown in **scheme 4.3.**

Complex 8

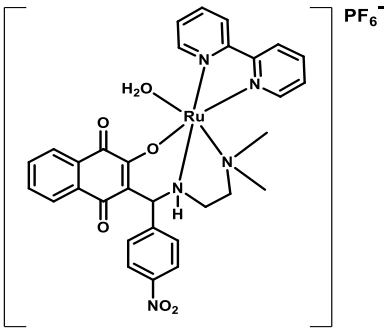

Brownish black; Yield: 58%; M.P: 178-182 ^{o}C

IR (KBr) cm^{-1}: 3480 (O-H), 3075 (C-H), 1645 (C=O), 1625 (C=N), 1601 (N=O), 1554 (δ N-H), 1345 (N=O), 1274 (C-O), 1160 (C-N), 843 (P-F), 557 (Ru-N), 484 (Ru-O)

(figure S4.5), ESI/MS 815.89 $[M+1]^+$ For $C_{31}H_{30}F_6N_5O_6PRu$ **(figure 4.3),** Anal. Calculated %: C, 45.89; H, 3.71; N, 8.6. Found %: C, 45.92; H, 3.65; N, 8.65 **UV-Vis (DMSO) λ/nm, (log ε):** 288 (7.837), 430 (6.781). **Molar conductance:** 87 S cm^2 mol^{-1}

Complex 9

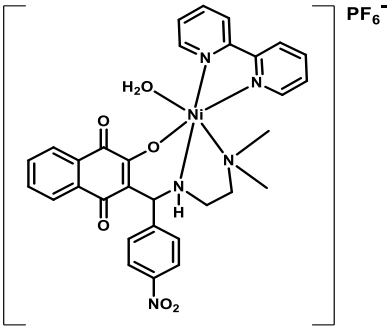

Radish brown; Yield: 64%; M.P: 158-162 ºC

IR (KBr) cm^{-1}: 3440 (O-H), 2927 (C-H), 1629 (C=N), 1588 (N=O), 1546 (δ N-H), 1346 (N=O), 1293 (C-O), 1160 (C-N), 844 (P-F) **(figure S4.6), ESI/MS** 625.30 $[M+1]^+$ For $C_{31}H_{30}N_5O_6Ni$ **(figure 4.4),** Anal. Calculated %: C, 59.36; H, 4.82; N, 11.16. Found %: C, 59.08; H, 4.40; N, 11.17 **UV-Vis (DMSO) λ/nm, (log ε):** 277 (1.928), 488 (6.696), 646 (6.249). **Molar conductance:** 95 S cm^2 mol^{-1}

4.5.4 Computational Studies

Theoretical calculations were carried out using Gaussian 16 software program and followed the procedure as depicted in **chapter 3 (section 3.4.4)**

4.5.5 DNA Binding Experiments

DNA is considered as the primary biological target on numerous antitumor drugs, a series of spectroscopic tools have been employed for the determination of in vitro binding modes and binding strength of the complexes towards DNA. All the experiments were performed in buffer solution (5 mM trisodium citrate and 50 mM NaCl at pH 7.4) at room temperature and followed the procedure as depicted in **chapter 3 (section 3.4.5)**

4.5.6 BSA binding experiments

BSA binding studies were carried out using protocol mentioned in **chapter 3 (section 3.4.6)**

4.5.7 Cytotoxicity assay

The cytotoxicity of the compounds on HepG2 cells was evaluated by the resazurin dye-based assay. 96 well plate was seeded with 1000 cells per well with culture growth media as follows: DMEM (Hyclone, GE) supplemented with 10% Fetal Bovine Serum (Gibco) and Antibiotic-Antimycotic (1x) (Thermo, USA). Following overnight incubation, the media was replaced with fresh media containing test compounds at various concentrations incubated for 72 hours in a humidified incubator at 37 °C and CO2 maintained at 5%. Test compounds were diluted in Dimethyl sulfoxide Hybri-Max™ (Sigma-Aldrich, USA) at 100mM concentration and serially diluted in growth media to obtain concentrations 1000 µM, 500 µM, 250 µM, 125 µM, 62.5 µM, 31.5 µM, 15.62 µM. Subsequently, cells were incubated with 1X Resazurin dye solution (100ug/ml) (Sigma-Aldrich, St. Louis, MO, USA) for 4 h, and fluorescence was measured at 530nm excitation/590nm emission on a Synergy HT microplate reader (BioTekInstruments, USA). The experiment was performed with three replicates for each concentration. IC_{50} values and Cytotoxicity graph was plotted using Quest Graph™ IC_{50} Calculator (AAT Bioquest).

4.5.8 Antimicrobial activity

The synthesized complexes were examined for their potential application in antimicrobial activity against two gram positive (Staphylococcus aureus, Bacillus subtilis) and two gram negative (Pseudomonas aeruginosa, Escherichia coli) bacterial strains. The Kirby-Bauer disk diffusion methodology employed with the nutrient agar medium for antimicrobial activity[59]. In the sterile autoclaved medium, the bacteria was subculture and incubated for up to 24 hours (37± 2°C). Chloramphenicol (30 µg/mL) and DMSO were taken as positive and negative control respectively. The stock solution of complexes and ligand (1 mg/mL) was prepared in DMSO. Following dilution of the stock solution, the antimicrobial activity of each compound was assessed at three different concentrations, namely 10, 50, and 100 µg/mL. The 5 mm-diameter discs were submerged in the test solutions of the aforementioned three concentrations, then set on a suitable nutrient medium that had already been seeded with organisms in petri plates and kept in an incubator throughout the aforementioned time. The inhibition area of microorganism were measured with the mm scale after 24h and reported.

4.5 Conclusion

Finally, using the oxygen and two nitrogen atoms (ONN) donor Mannich base ligand, unique V(IV), Ru(II), and Ni(II) metal complexes were successfully synthesized. Different methods, such as molar conductivity, spectroscopic, and analytical approaches, were used to characterize the ligand and complexes (1H NMR, 13C NMR, Uv-Visible, FT-IR, ESI-MS and ESR). Bond length, bond angle, HUMO and LUMO energy gaps (E), among other crucial geometry optimization parameters, were also established. It is feasible to conclude that the successful synthesis of metal complexes under particular circumstances from these various spectroscopic analyses. UV-visible and fluorescence spectroscopy were used to confirm the intercalative and groove binding interactions of complexes with biomolecules such as CT-DNA and BSA. All available spectroscopic techniques demonstrated unequivocally that V(IV) and Ru(II) complexes exhibit the strongest binding with both DNA and BSA, but Ni(II) complex showed only modest contact. DFT research backed up the experimental results. The cytotoxicity potential of ligand and complexes was assessed using a resazurin dye-based assay on HepG2 cells, and the results showed that the ruthenium complex had significantly higher activity than ligand and other complexes, and that it was comparable to standard medication. In vitro antibacterial test results also revealed that the generated **complexes 7** and **8** performed better than the **19** in terms of antibacterial activity and were equivalent to standard drugs.

4.6 Spectra

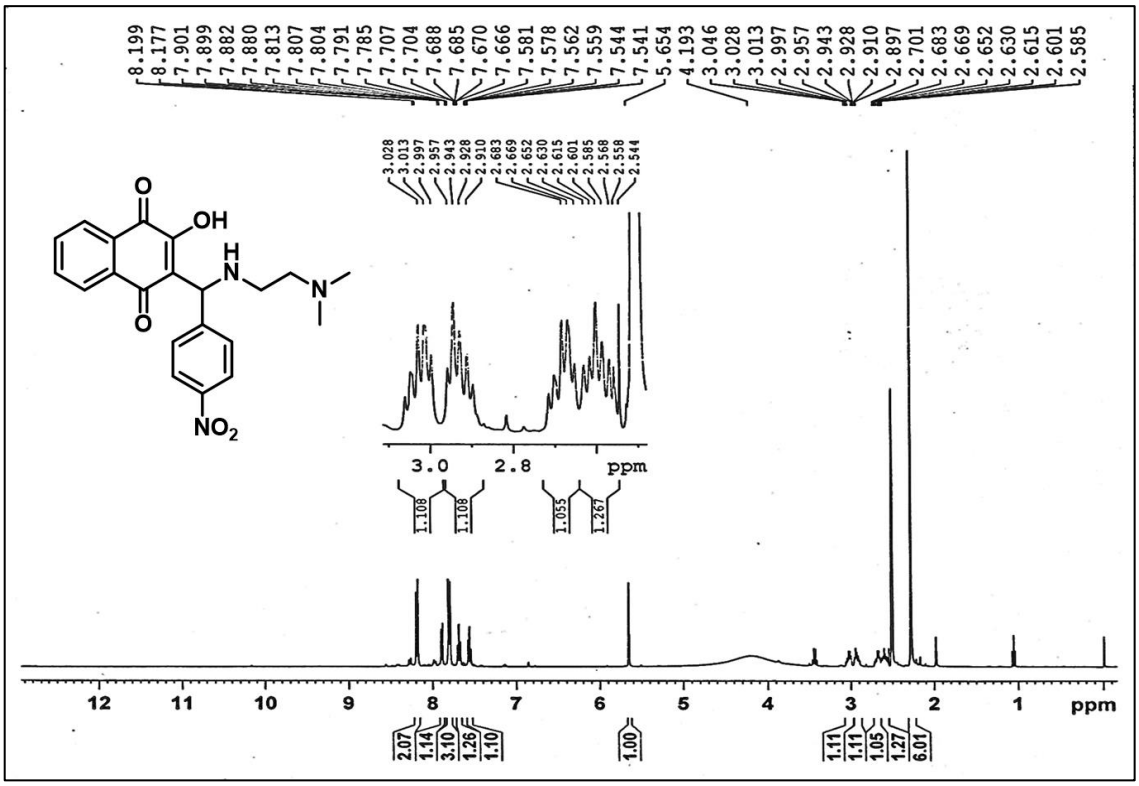

Figure S4.1 ^{1}H NMR spectra of 19

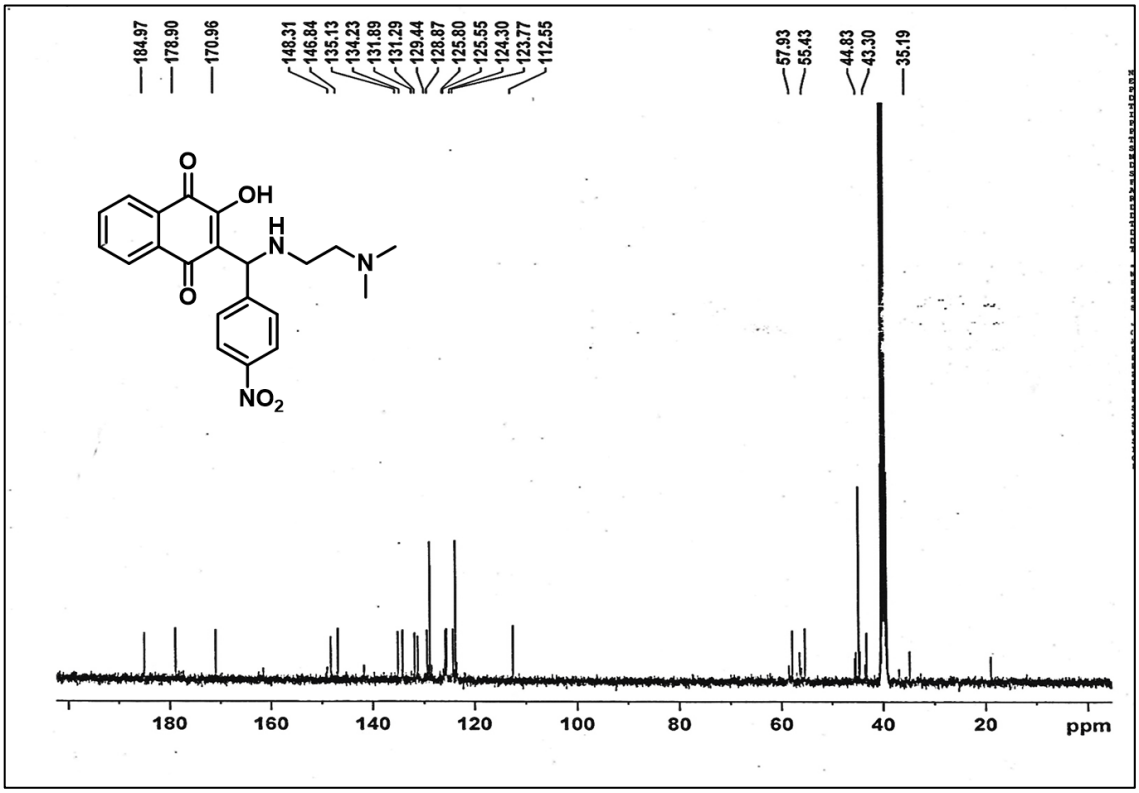

Figure S4.2 ^{13}C NMR spectra of 19

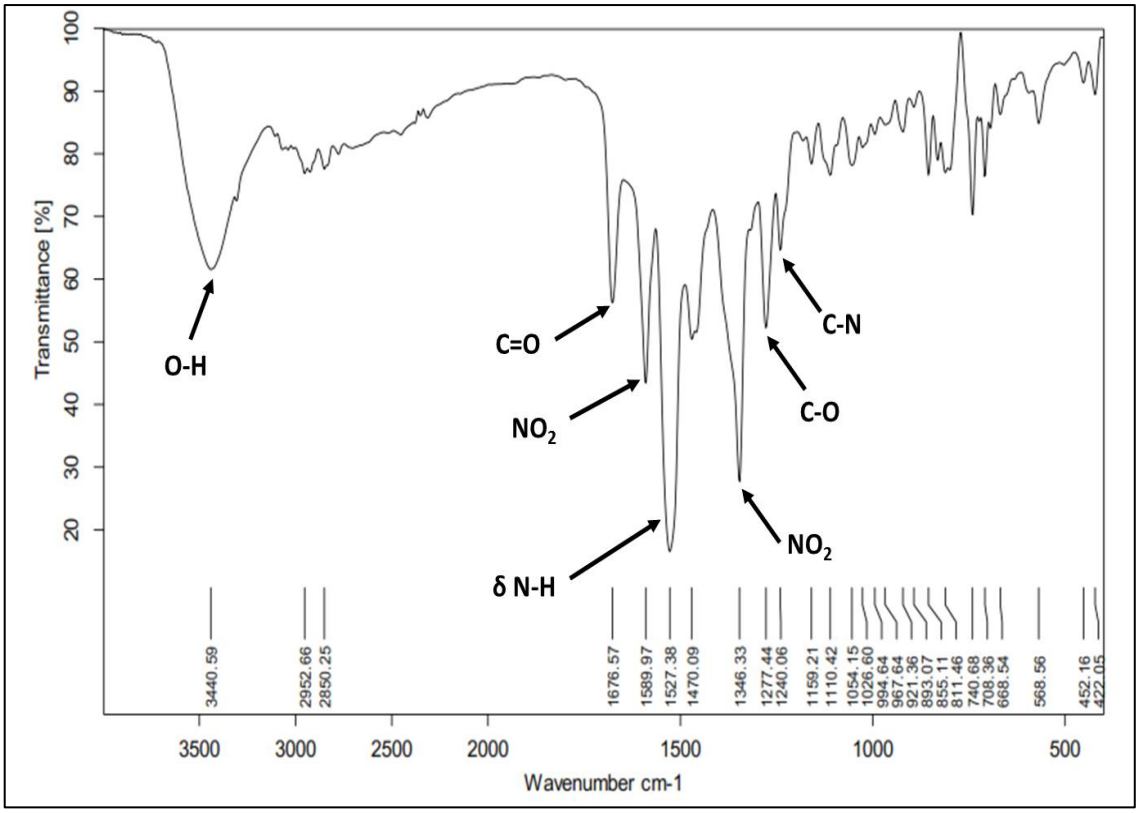

Figure S4.3 FT-IR spectra of 19

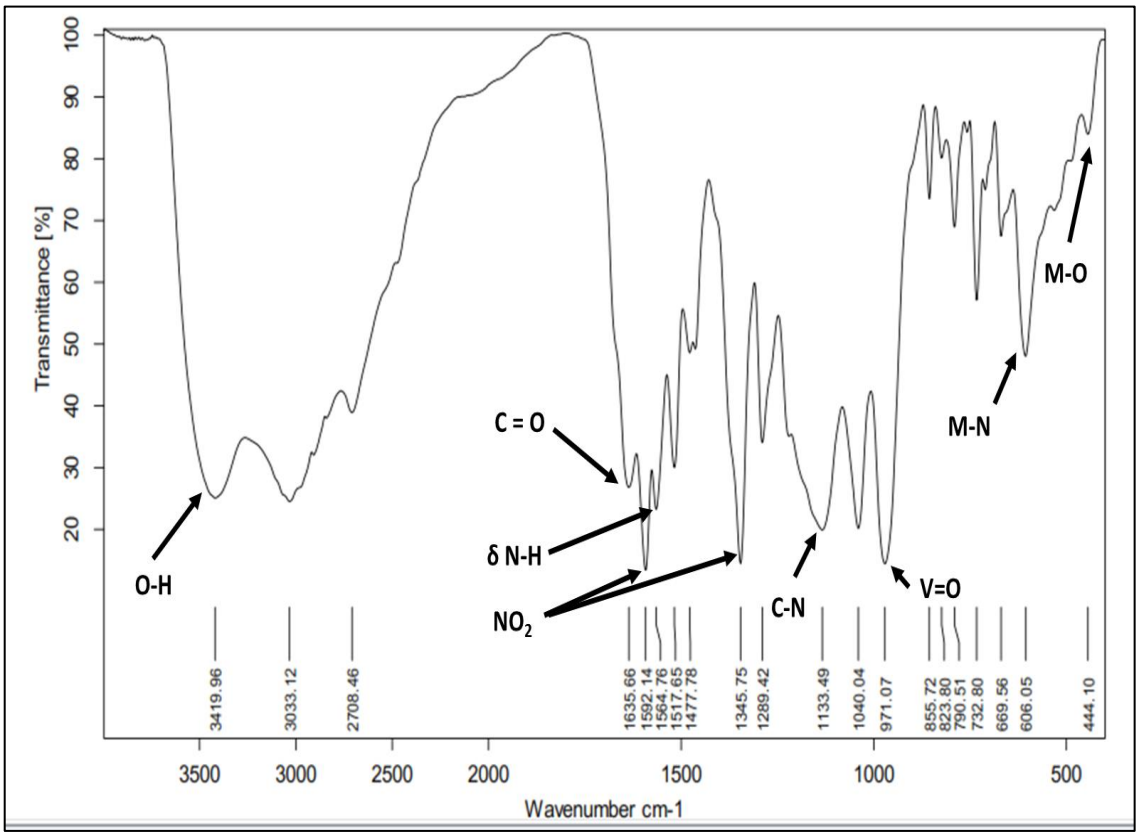

Figure S4.4 FT-IR spectra of complex 7

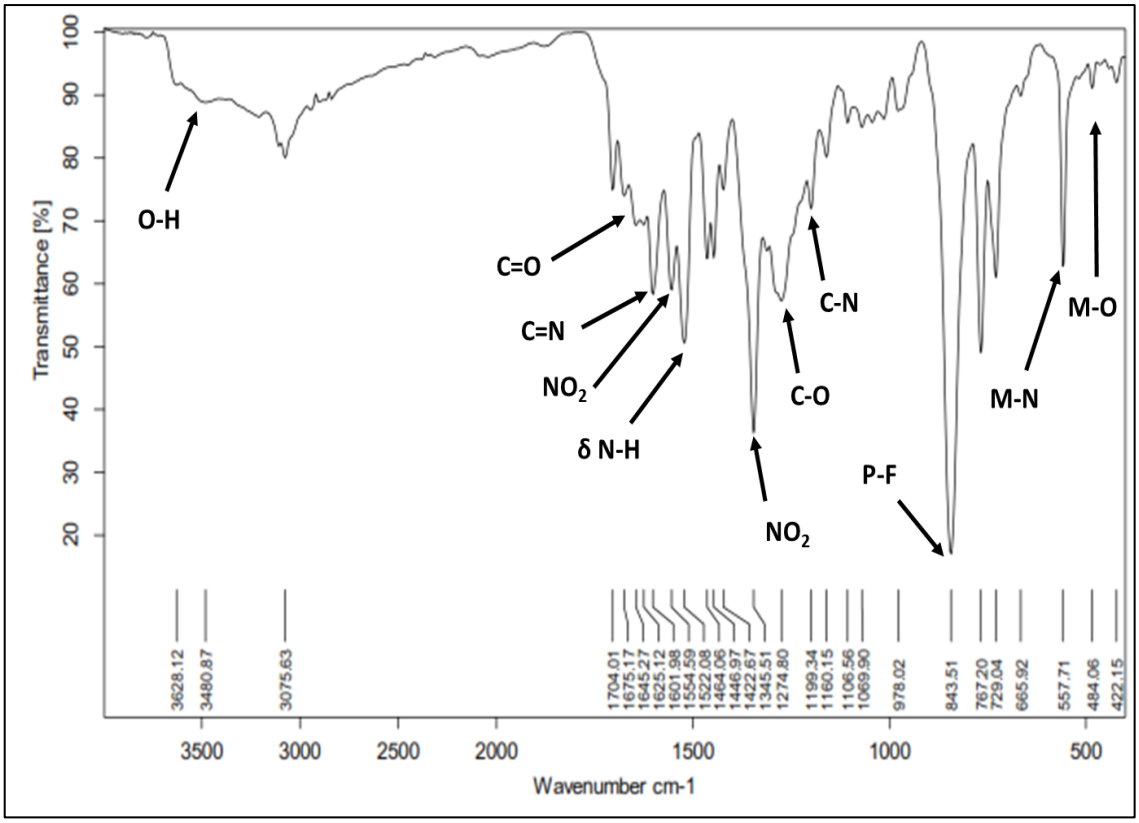

Figure S4.5 FT-IR spectra of complex 8

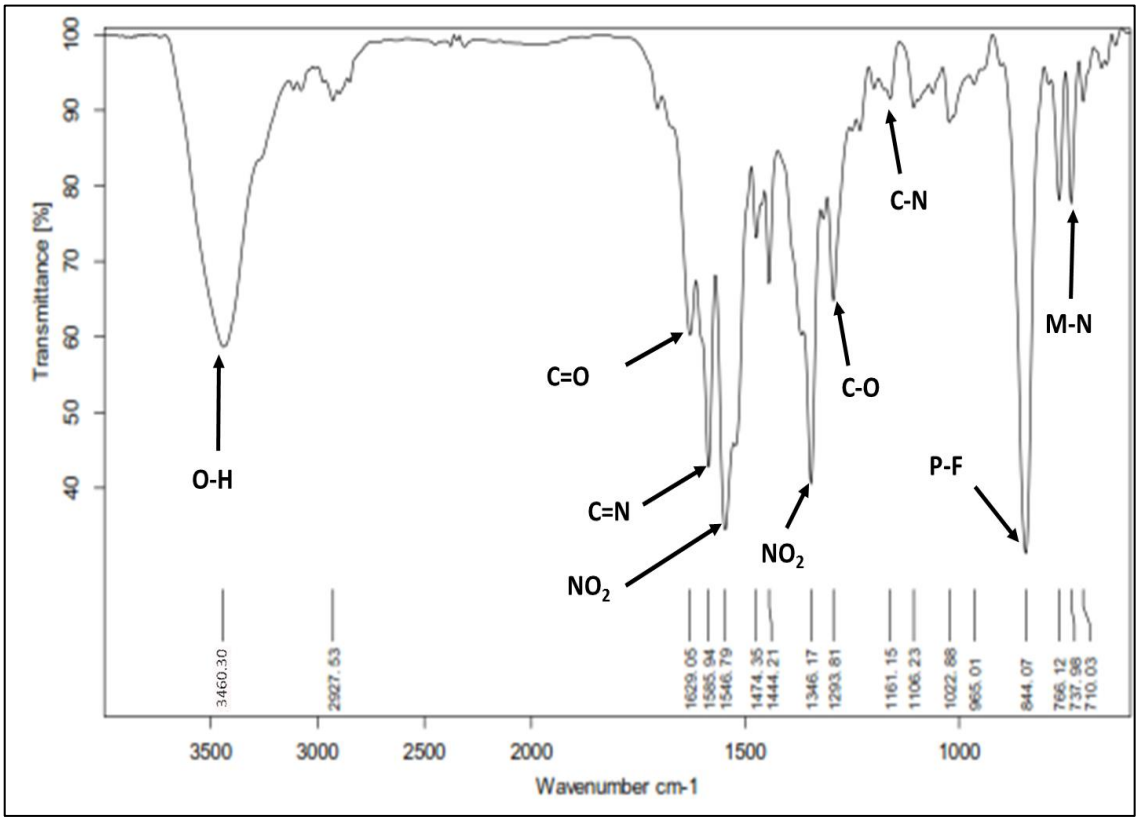

Figure S4.6 FT-IR spectra of complex 9

4.7 References

1. Hamdani, H. EL & Amane, M. EL. Preparation, spectral, antimicrobial properties and anticancer molecular docking studies of new metal complexes [M(caffeine) 4] (PF 6) 2; M = Fe(II), Co(II), Mn(II), Cd(II), Zn(II), Cu(II), Ni(II). *J. Mol. Struct.* **1184**, 262–270 (2019).

2. Kelland, L. The resurgence of platinum-based cancer chemotherapy. *Nat. Rev. Cancer* **7**, 573–584 (2007).

3. Nagesh, G. Y., Mahendra Raj, K. & Mruthyunjayaswamy, B. H. M. Synthesis, characterization, thermal study and biological evaluation of Cu(II), Co(II), Ni(II) and Zn(II) complexes of Schiff base ligand containing thiazole moiety. *J. Mol. Struct.* **1079**, 423–432 (2015).

4. El-Gammal, O. A., Mohamed, F. S., Rezk, G. N. & El-Bindary, A. A. Structural characterization and biological activity of a new metal complexes based of Schiff base. *J. Mol. Liq.* **330**, 115522 (2021).

5. Ali, I. A. I., El-Sakka, S. S. A., Soliman, M. H. A. & Mohamed, O. E. A. In silico, In Vitro and docking applications for some novel complexes derived from new quinoline derivatives. *J. Mol. Struct.* **1196**, 8–32 (2019).

6. Datta, C. *et al.* Novel water soluble neutral vanadium(IV)-antibiotic complex: Antioxidant, immunomodulatory and molecular docking studies. *Eur. J. Med. Chem.* **97**, 214–224 (2015).

7. Carreño, A. *et al.* Study of the structure-bioactivity relationship of three new pyridine Schiff bases: Synthesis, spectral characterization, DFT calculations and biological assays. *New J. Chem.* **42**, 8851–8863 (2018).

8. Singla, M., Ranjan, R., Mahiya, K., Mohapatra, S. C. & Ahmad, S. Nitric oxide inhibition, antioxidant, and antitumour activities of novel copper(ii) bis-benzimidazole diamide nanocoordination complexes. *New J. Chem.* **39**, 4316–4327 (2015).

9. Abumelha, H. M. *et al.* Synthesis and characterization for pharmaceutical models from Co(II), Ni(II) and Cu(II)-thiophene complexes; apoptosis, various theoretical studies and pharmacophore modeling. *J. Mol. Liq.* **328**, (2021).

10. Li, L., Guo, Q., Dong, J., Xu, T. & Li, J. DNA binding, DNA cleavage and BSA interaction of a mixed-ligand copper(II) complex with taurine Schiff base and 1,10-phenanthroline. *J. Photochem. Photobiol. B Biol.* **125**, 56–62 (2013).

11. Parveen, S., Premkumar, T., Nguyen, H. H. & Govindarajan, S. Facile template synthesis of water-soluble triazine-based Schiff base ligand bridged-coordination polymers of Co(ii), Ni(ii), and Cu(ii): Structure, biomolecular interactions, and cytotoxic activity. *New J. Chem.* **43**, 13371–13380 (2019).

12. Mondal, A. *et al.* Biological promiscuity of a binuclear Cu(ii) complex of aminoguanidine Schiff base: DNA binding, anticancer activity and histidine sensing ability of the complex. *New J. Chem.* **44**, 7319–7328 (2020).

13. Hassan, M. A., Omer, A. M., Abbas, E., Baset, W. M. A. & Tamer, T. M. Preparation, physicochemical characterization and antimicrobial activities of novel two phenolic chitosan Schiff base derivatives. *Sci. Rep.* **8**, 1–14 (2018).

14. Zehra, S., Shavez Khan, M., Ahmad, I. & Arjmand, F. New tailored substituted benzothiazole Schiff base Cu(II)/Zn(II) antitumor drug entities: effect of substituents on DNA binding profile, antimicrobial and cytotoxic activity. *J. Biomol. Struct. Dyn.* **37**, 1863–1879 (2019).

15. Al-Hazmi, G. A. A. *et al.* Synthesis and structural characterization of oxovanadium(IV) complexes of dimedone derivatives. *Appl. Organomet. Chem.* **34**, 1–16 (2020).

16. Adam, M. S. S. & Elsawy, H. Biological potential of oxo-vanadium salicylediene amino-acid complexes as cytotoxic, antimicrobial, antioxidant and DNA interaction. *J. Photochem. Photobiol. B Biol.* **184**, 34–43 (2018).

17. Sheikhshoaie, I., Ebrahimipour, S. Y., Lotfi, N., Mague, J. T. & Khaleghi, M. Synthesis, spectral characterization, X-ray crystal structure and antimicrobial activities of two cis dioxido-vanadium(V) complexes incorporating unsymmetrical dimalonitrile-based (NNO) Schiff base ligands. *Inorganica Chim. Acta* **442**, 151–157 (2016).

18. Kongot, M. *et al.* Oxidovanadium (IV) and iron (III) complexes with O2N2 donor linkage as plausible antidiabetic candidates: Synthesis, structural characterizations, glucose uptake and model biological media studies. *Appl. Organomet. Chem.* **34**, 1–12 (2020).

19. Ali, S., Singh, V., Jain, P. & Tripathi, V. Synthesis, antibacterial, anticancer and molecular docking studies of macrocyclic metal complexes of dihydrazide and diketone. *J. Saudi Chem. Soc.* **23**, 52–60 (2019).

20. Thota, S., Rodrigues, D. A., Crans, D. C. & Barreiro, E. J. Ru(II) Compounds: Next-Generation Anticancer Metallotherapeutics? *J. Med. Chem.* **61**, 5805–5821 (2018).

21. Flamme, M., Clarke, E., Gasser, G. & Hollenstein, M. Applications of ruthenium complexes covalently linked to nucleic acid derivatives. *Molecules* **23**, 28–31 (2018).

22. Elsayed, S. A., Badr, H. E., di Biase, A. & El-Hendawy, A. M. Synthesis, characterization of ruthenium(II), nickel(II), palladium(II), and platinum(II) triphenylphosphine-based complexes bearing an ONS-donor chelating agent:

Interaction with biomolecules, antioxidant, in vitro cytotoxic, apoptotic activity and cell . *J. Inorg. Biochem.* **223**, 111549 (2021).

23. Romero-Canelón, I. & Sadler, P. J. Next-generation metal anticancer complexes: Multitargeting via redox modulation. *Inorg. Chem.* **52**, 12276–12291 (2013).

24. Neves, A. P. *et al.* Novel zinc(II) and copper(II) complexes of a Mannich base derived from lawsone: Synthesis, single crystal X-ray analysis, ab initio density functional theory calculations and vibrational analysis. *Spectrochim. Acta - Part A Mol. Biomol. Spectrosc.* **94**, 152–163 (2012).

25. Neves, A. P. *et al.* Novel aminonaphthoquinone Mannich bases derived from lawsone and their copper(II) complexes: Synthesis, characterization and antibacterial activity. *J. Braz. Chem. Soc.* **20**, 712–727 (2009).

26. Oliveira, K. M. *et al.* Selective Ru(II)/lawsone complexes inhibiting tumor cell growth by apoptosis. *J. Inorg. Biochem.* **176**, 66–76 (2017).

27. Indira, S., Vinoth, G., Bharathi, M. & Shanmuga Bharathi, K. Synthesis, spectral, electrochemical, in-vitro antimicrobial and antioxidant activities of bisphenolic mannich base and 8-hydroxyquinoline based mixed ligands and their transition metal complexes. *J. Mol. Struct.* **1198**, 126886 (2019).

28. Yang, P. *et al.* Copper(ii) complexes with NNO ligands: Synthesis, crystal structures, DNA cleavage, and anticancer activities. *Dalt. Trans.* **48**, 17925–17935 (2019).

29. Yuan, C. *et al.* Synthesis, characterization, and protein tyrosine phosphatases inhibition activities of oxovanadium(IV) complexes with Schiff base and polypyridyl derivatives. *J. Inorg. Biochem.* **104**, 978–986 (2010).

30. Tyagi, P., Chandra, S., Saraswat, B. S. & Yadav, D. Design, spectral characterization, thermal, DFT studies and anticancer cell line activities of Co(II), Ni(II) and Cu(II) complexes of Schiff bases derived from 4-amino-5-(pyridin-4-yl)-4H-1,2,4-triazole-3-thiol. *Spectrochim. ACTA PART A Mol. Biomol. Spectrosc.* (2015) doi:10.1016/j.saa.2015.03.034.

31. Gerasimova, T. P. & Katsyuba, S. A. Bipyridine and phenanthroline IR-spectral bands as indicators of metal spin state in hexacoordinated complexes of Fe(II), Ni(II) and Co(II). *Dalt. Trans.* **42**, 1787–1797 (2013).

32. Arjmand, F., Afsan, Z. & Roisnel, T. Design, synthesis and characterization of novel chromone based-copper(ii) antitumor agents with N,N-donor ligands: comparative DNA/RNA binding profile and cytotoxicity. *RSC Adv.* **8**, 37375–37390 (2018).

33. Loganathan, R. *et al.* DNA and protein binding, double-strand DNA cleavage and cytotoxicity of mixed ligand copper(II) complexes of the antibacterial drug

nalidixic acid. *J. Inorg. Biochem.* **174**, 1–13 (2017).

34. Khadtare, S. S. *et al.* Dye sensitized solar cell with lawsone dye using a ZnO photoanode: Experimental and TD-DFT study. *RSC Adv.* **5**, 17647–17652 (2015).

35. Sallam, S. A., Orabi, A. S. & Abbas, A. M. DNA interaction with octahedral and square planar Ni(II) complexes of aspartic-acid Schiff-bases. *J. Mol. Struct.* **1006**, 272–281 (2011).

36. Zhu, S. S., Dong, X. & Zhou, Z. H. Mixed ligand oxidovanadium(IV) complexes: Synthesis, spectral, structural characterization and catalytic degradations of methyl orange. *Inorganica Chim. Acta* **486**, 395–400 (2019).

37. Garribba, E., Micera, G., Panzanelli, A. & Sanna, D. Electronic Structure of Oxovanadium(IV) Complexes of α-Hydroxycarboxylic Acids. *Inorg. Chem.* **42**, 3981–3987 (2003).

38. J, D. Synthesis, Crystal Structure, and Electronic Properties of (L-Methionylglycinato)copper(II). *Inorg. Chem.* **18**, 1543 (1979).

39. Syiemlieh, I., Asthana, M., Kurbah, S. D. & Lal, R. A. Synthesis, crystal structure and reactivity of homobimetallic vanadium(V) complexes derived from oxaloyldihydrazone ligands. *Polyhedron* **170**, 202–216 (2019).

40. Borah, R., Lahkar, S., Deori, N. & Brahma, S. Synthesis, characterization and application of oxovanadium(iv) complexes with [NNO] donor ligands: X-ray structures of their corresponding dioxovanadium(v) complexes . *RSC Adv.* **12**, 13740–13748 (2022).

41. Gurusamy, S., Krishnaveni, K., Sankarganesh, M., Nandini Asha, R. & Mathavan, A. Synthesis, characterization, DNA interaction, BSA/HSA binding activities of VO(IV), Cu(II) and Zn(II) Schiff base complexes and its molecular docking with biomolecules. *J. Mol. Liq.* **345**, 117045 (2022).

42. Maurya, M. R., Uprety, B., Avecilla, F., Adão, P. & Pessoa, J. C. Vanadium(V) complexes of a tripodal ligand, their characterisation and biological implications. 17736–17755 (2015) doi:10.1039/c5dt02716k.

43. Maurya, A. *et al.* Synthesis and characterization of dimeric μ-oxidovanadium complexes as the functional model of vanadium bromoperoxidase. *Appl. Organomet. Chem.* **34**, 1–21 (2020).

44. Murugavel, S., Ravikumar, C., Jaabil, G. & Alagusundaram, P. Synthesis, crystal structure analysis, spectral investigations (NMR, FT-IR, UV), DFT calculations, ADMET studies, molecular docking and anticancer activity of 2-(1-benzyl-5-methyl-1H-1,2,3-triazol-4-yl)-4-(2-chlorophenyl)-6-methoxypyridine – A novel poten. *J. Mol. Struct.* **1176**, 729–742 (2019).

45. Krishnan, K. G. *et al.* Novel cyanoacetamide integrated phenothiazines: Synthesis, characterization, computational studies and in vitro antioxidant and anticancer evaluations. *J. Mol. Struct.* **1199**, 127037 (2020).

46. Khan, I. M. *et al.* Exploring interaction dynamics of designed organic cocrystal charge transfer complex of 2-hydroxypyridine and oxalic acid with human serum albumin: Single crystal, spectrophotometric, theoretical and antimicrobial studies. *Bioorg. Chem.* **100**, 103872 (2020).

47. Rocha, M. *et al.* Diethylaminophenyl-based Schiff base Cu(ii) and V(iv) complexes: Experimental and theoretical studies and cytotoxicity assays. *New J. Chem.* **43**, 18832–18842 (2019).

48. Kumar, M., Kumar, G. & Masram, D. T. Copper(ii) complexes containing enoxacin and heterocyclic ligands: Synthesis, crystal structures and their biological perspectives. *New J. Chem.* **44**, 8595–8613 (2020).

49. Draksharapu, A. *et al.* Binding of Copper(II) Polypyridyl Complexes to DNA and Consequences for DNA-based Asymmetric Catalysis. *Dalt. Trans.* **44**, 3647–3655 (2015).

50. Zampakou, M. *et al.* Structure, antimicrobial activity, albumin- and DNA-binding of manganese(<scp>ii</scp>)–sparfloxacinato complexes. *RSC Adv.* **5**, 11861–11872 (2015).

51. Mudavath, R. *et al.* Molecular docking, QSAR properties and DNA/BSA binding, anti-proliferative studies of 6-methoxy benzothiozole imine base and its metal complexes. *J. Biomol. Struct. Dyn.* **38**, 2849–2864 (2020).

52. Kumar, M., Kumar, G., Dadure, K. M. & Masram, D. T. Copper(II) complexes based on levofloxacin and 2N-donor ligands: synthesis, crystal structures and in vitro biological evaluation. *New J. Chem.* **43**, 15462–15481 (2019).

53. Niu, M. *et al.* DNA/protein interaction, cytotoxic activity and magnetic properties of amino-alcohol Schiff base derived Cu(ii)/Ni(ii) metal complexes: influence of the nuclearity and metal ions. *RSC Adv.* **5**, 37085–37095 (2015).

54. Sathyadevi, P. *et al.* Effect of substitution and planarity of the ligand on DNA/BSA interaction, free radical scavenging and cytotoxicity of diamagnetic Ni(ii) complexes: A systematic investigation. *Dalt. Trans.* **40**, 9690 (2011).

55. Krishnamoorthy, P. *et al.* Copper(i) and nickel(ii) complexes with 1 : 1 vs. 1 : 2 coordination of ferrocenyl hydrazone ligands: Do the geometry and composition of complexes affect DNA binding/cleavage, protein binding, antioxidant and cytotoxic activities? *Dalt. Trans.* **41**, 4423 (2012).

56. Joksimović, N. *et al.* Synthesis, characterization, biological activity, DNA and BSA binding study: Novel copper(II) complexes with 2-hydroxy-4-aryl-4-oxo-2-

butenoate. *Dalt. Trans.* **45**, 15067–15077 (2016).

57. Gomathi Sankareswari, V. *et al.* Interaction of oxovanadium(iv)–salphen complexes with bovine serum albumin and their cytotoxicity against cancer. *Dalt. Trans.* **43**, 3260–3272 (2014).

58. Pascale, F., Bedouet, L., Baylatry, M., Namur, J. & Laurent, A. Comparative chemosensitivity of VX2 and HCC cell lines to drugs used in TACE. *Anticancer Res.* **35**, 6497–6504 (2015).

59. Balouiri, M., Sadiki, M. & Ibnsouda, S. K. Methods for in vitro evaluating antimicrobial activity: A review. *J. Pharm. Anal.* **6**, 71–79 (2016).